Simulation-Based Assessment of Proton Radiography Across Energy Levels: Investigations on optimum imaging energy

Aurelija Vinke*

Riga Technical University, Faculty of Mechanical Engineering, Transport and Aeronautics, Bachelor's Program in Medical Engineering and Physics, Riga, Latvia

Kristaps Palskis

CERN, Doctoral Program, Institute of Particle Physics and Accelerator Technologies, Riga, Latvia †

Maurizio Vretenar

CERN, NIMMS Group Leader ‡

(Dated: September 2024)

I. INTRODUCTION

Proton therapy (PT) is a highly precise radiotherapy method that significantly reduces radiation exposure to healthy tissues by [1] 30-50%, making it particularly valuable for treating tumors near critical organs. Similarly,[2] helium ion therapy has emerged as an alternative that offers even greater precision owing to the heavier mass of helium ions. However, both proton and helium ion therapies face the common challenge of accurately determining the position of the Bragg peak, where most of the energy is deposited. Precise dose distribution is necessary, as the sharp Bragg peak makes these therapies more sensitive to treatment uncertainties than conventional photon therapies.

Uncertainties arise from multiple factors, including patient-specific aspects, such as anatomical changes and physiological motion, as well as physical interactions of particle beams with matter, particularly in the calculation of relative stopping power (RSP). [3] The uncertainty in the general range generally lies between 3% and 5%, which can significantly affect the precision of the treatment. Proton radiography (PR) has been explored as a method that can help improve the precision of the location of the Bragg peak by providing more accurate images of the internal structure of a patient during treatment.

PR builds on PT by providing high-resolution rapid imaging, which is particularly useful for thick [4] imaging systems (up to 100 g/cm^2). As protons pass through matter, they undergo nuclear and small-angle Coulomb scattering, as well as energy loss, which depends on the properties of the material. These interactions enable PR to measure and identify material composition, making it adaptable for a range of thicknesses.

However, protons are more sensitive to anatomical changes and motion than photons. [5] Multiple Coulomb scattering (MCS) can degrade spatial resolution by altering proton trajectories, especially when imaging thick or high-density materials, leading to blurring. Managing the effects of MCS and anatomical variability is critical to achieving optimal image clarity.

[6]High-energy protons offer a potential solution by reducing the effects of MCS because they are less prone to deflection. This leads to more precise proton trajectories and improved spatial resolution, particularly for dense materials. Therefore, using higher-energy protons

* aurelija.vinke@rtu.lv

† kristaps.palskis@rtu.lv

‡ maurizio.vretenar@cern.ch

could enhance the PR image quality by mitigating the MCS effects.

This study investigates whether higher-energy protons generated by the compact helium synchrotron developed by CERN NIMMS provide a physical advantage for PR. The proton beam energies of 250, 330, 400, 500, 600, and 700 MeV were selected based on previous work (specifically 250 and 330 MeV) and the design capabilities of the [7] NIMMS HeLICS system. The selected energies were tested in two anatomical models [8]: one representing a head-shaped structure with a depth of 16 cm and another representing thicker anatomy, such as the pelvis, with a depth of 32 cm. These high-energy beams offer the potential to improve imaging in both anatomical regions by addressing the issue of range straggling and improving the dose accuracy.

II. METHODOLOGY

This study used six proton beam energies (250, 330, 400, 500, 600, and 700 MeV) to evaluate their effects on PR. The selection of 250 and 330 MeV was based on previous research, whereas the higher energies were chosen according to the design capabilities of the NIMMS HeLICS system. Two homogeneous water phantoms were used to simulate anatomical regions: a depth of 16 cm representing head anatomy and a depth of 32 cm representing pelvis. These depths provide a basis for assessing the spatial and contrast resolutions at various proton energies, enabling a comprehensive analysis of the effects of energy on PR performance.

The simulation framework was developed using [9]Geant4, which was configured to model proton interactions with phantoms. All relevant parameters, including energy levels, directionality, and interaction models, were defined to ensure accurate simulation conditions. The spatial resolution was evaluated using an aluminum cube, while the contrast resolution was evaluated using cylindrical tissue equivalent materials representing different human tissues.

Key calculations included determining the [10] Water Equivalent Path Length (WEPL) by transforming the outgoing kinetic energies of the particles into WEPL values traversed by each particle.[10] The Most Likely Path (MLP) formalism was applied to reconstruct 2D images while accurately accounting for proton trajectories, and the Most Likely Path (MLP) formalism was applied. Multiple data filtration techniques were used before image reconstruction for the precise implementation of the MLP formalism. These include energy filtering, particle count filtering, and relative angle filtering, with pixel-wise energy filtering implemented to enhance the accuracy of the reconstructed images in more complex geometries.

A. Simulation Setup

1. *Phantom Design and Materials*

To accurately model proton beam interactions, homogeneous water phantoms were designed to represent both thin and thick tissue regions. These phantoms were selected to assess the influence of varying depths on proton beam propagation and image quality.

Two primary materials were used in the simulation, G4_WATER (water) and G4_AIR (air). Water was selected as the target material due to its well-characterized atomic composition and density (1 g / cm3), making it a standard reference material for medically relevant ionizing radiation studies. Air, with its low density (0.0012 g / cm3), was used for the world volume, detector, and check volumes to minimize interference with particle motion and ensure accurate simulation results.

In addition, various materials were chosen to represent different types of human tissue, including the lung, brain, muscle, adipose tissue, and bone. The physical properties of these materials, such as the atomic number (Z), atomic mass (A), mean excitation energy (I), and density, were sourced from the database [11] National Institute of Standards and Technology (NIST). The properties are listed in Table I.

TABLE I: Material Properties Utilized in Simulations (Sourced from NIST Database)

Material	Z	A	I (MeV)	Density (g/cm^3)
G4_BRAIN_ICRP	6.922	13.73751	73.3	1.04
G4_ADIPOSE_TISSUE_ICRP	6.019	11.93346	63.2	0.95
G4_MUSCLE_STRIATED_ICRU	7.09	14.08	74.7	1.04
G4_BONE_COMPACT_ICRU	9.177	18.37168	85.9	1.85
G4_LUNG_ICRP	6.987	13.87546	75.3	0.26
G4_BONE_CORTICAL_ICRP	10.795	21.63329	110	1.92
G4_WATER	7.51	15.9994	78.0	1.0
G4_AIR	7.78	14.464	85.7	0.0012
G4_Al	13.0	26.9815	166.0	2.7

2. High-Contrast Object for Spatial Resolution

To evaluate the spatial resolution achievable with the different energies studied, a high-contrast object, specifically an aluminum cube with dimensions of $2 \times 2 \times 2$ cm, was introduced into the water phantom. [10]The selection of aluminum was based on its material properties, which differ significantly from those of water. With an atomic number of 13 and a density of 2.7 g/cm^3, aluminum provides substantial contrast compared to water, which has a lower atomic number (approximately 7.5) and density (1 g/cm^3). The aluminum cube was centrally positioned at the point of interest in the middle of the phantom, with coordinates (0,0,0).

A 10×10 cm irradiation field was employed to ensure uniform exposure of the aluminum cube and its surrounding area. This field size is a [12]standard reference in clinical practice, providing a balance between adequate coverage of the target and minimizing scatter, thereby enhancing the accuracy of the dose distribution in the simulation.

3. Low Contrast Resolution Evaluation

After establishing the spatial resolution with the aluminum cube, the next step was to evaluate the [6]low contrast resolution, which complements the spatial resolution by demonstrating the ability of the simulation to differentiate materials with varying densities.

The materials selected for testing included lung, brain, muscle, adipose tissue, and bone, which were chosen for their relevance to human tissue. The RSP of each material was calculated relative to that of water (G4_WATER) to assess their interactions with proton beams. Cylinder thicknesses were carefully calculated and adjusted to ensure consistent contrast levels at different phantom depths. The thicknesses of the materials at both depths are listed in [13] Table II.

TABLE II: Cylinder Thicknesses and Relative Contrast Values of Selected Materials at 16 cm and 32 cm Depths

Material	Cylinder Thickness (16 cm depth)	Cylinder Thickness (32 cm depth)	Contrast Relative to Water
G4_LUNG_ICRP (-1%)	2 mm	4 mm	-1%
G4_LUNG_ICRP (-2.5%)	5 mm	11 mm	-2.5%
G4_ADIPOSE_TISSUE_ICRP	15 mm	31 mm	-0.5%
G4_BRAIN_ICRP	32 mm	64 mm	+0.5%
G4_MUSCLE_STRIATED_ICRU	45 mm	90 mm	+1%
G4_BONE_COMPACT_ICRU	5 mm	11 mm	+2.5%

This table lists the cylinder thicknesses required for each material to achieve detectable contrast with water at two phantom depths (16 and 32 cm). Contrast values, expressed as percentages of water (G4_WATER), represent the relative stopping power of each material, with negative values indicating a lower stopping power than water and positive values indicating a higher stopping power.

4. Material Configuration and Visualization

The selected materials were arranged in cylindrical form within a lattice configuration consisting of six rows and six columns. [13] The cylinder diameters (in mm) were organized in the following descending order: 15, 10, 7, 4, 2, and 0.5. Each column contains different materials with the corresponding contrasts, as shown in Figure 1, which illustrates the phantom at a depth of 16 cm. A three-dimensional (3D) side view of the cylinders is shown in Figure 2, offering a clear visualization of their spatial arrangement and depth distribution. This setup was designed to consistently and accurately evaluate the ability of the simulation to replicate tissue contrast at varying depths.

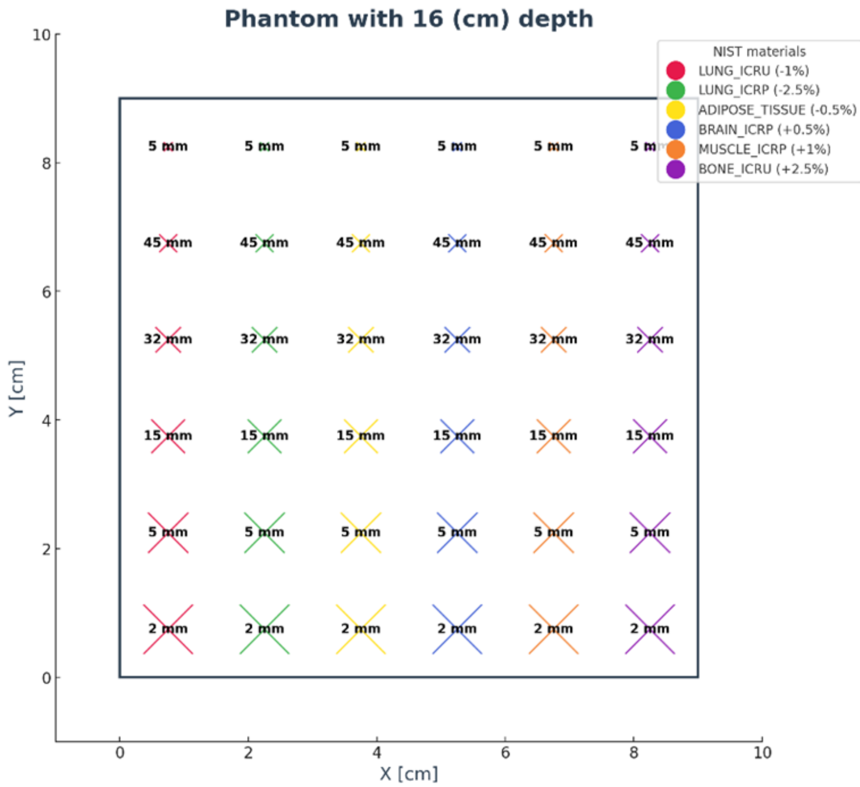

FIG. 1: Phantom Configuration at 16 cm Depth for Low-Contrast Resolution Analysis. This image illustrates the symmetrical arrangement of the cylinders within the phantom at a depth of 16 cm. The grid consisted of six rows and six columns, with cylinder diameters arranged in descending order: 15, 10, 7, 4, 2, and 0.5 mm. Each color represents a different human tissue analog, as indicated in the legend: LUNG_ICRU (-1%), LUNG_ICRP (-2.5%), ADIPOSE_TISSUE (-0.5%), BRAIN_ICRP (+0.5%), MUSCLE_ICRP (+1%), and BONE_ICRU (+2.5%). This setup evaluates the simulation's ability to resolve contrast across different tissue types and thicknesses, offering insights into tissue differentiation at both shallow and deep regions.

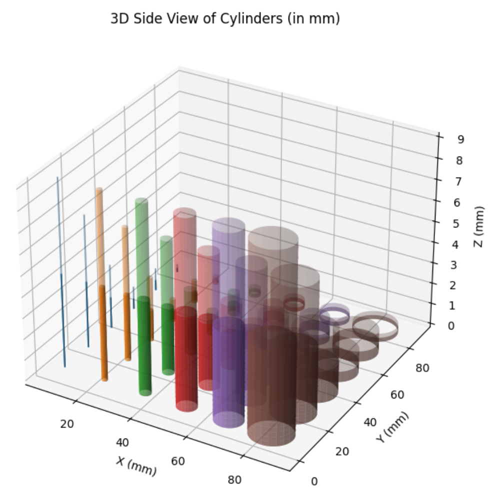

FIG. 2: 3D Side View of Cylindrical Materials for Contrast Resolution Testing. This figure shows a three-dimensional side view of the cylindrical materials arranged in the phantom for contrast resolution analysis. The cylinders were organized in a lattice configuration, with diameters decreasing from the front to the back. Each color represents a different tissue analog, with specific contrast values relative to that of water. The vertical axis (Z) corresponds to the cylinder height, whereas the X- and Y-axes display their positions within the grid. The 3D perspective clarifies the spatial arrangement and depth distribution of materials. Note: The cylinders appear as rings owing to rendering, but they are solid representations in the simulation.

B. Geant4 Simulation Framework

1. *Simulation Framework and Adjustments*

Simulations were conducted using Geant4 release 11.0.1, with adaptations tailored to the requirements of this study. With the source code vaguely based on the Geant4 Hard01 example, the framework was significantly modified to align it with the research objectives. The simulations were performed on a high-performance computing [14](HPC) cluster at Riga Technical University (RTU).

Key adjustments involved customizing the detector structure to define the phantom and detector geometries and ensuring accurate spatial configuration and material properties. A structured output file system was developed to streamline data analysis, capturing parameters such as energy, direction vectors, and spatial coordinates. Appropriate physical models for the hadronic and electromagnetic interactions were selected, and the initial beam conditions (source position, energy distribution, and trajectory) were defined to account for a more realistic and clinically relevant environment.

2. *Physics Models and Interactions*

The `QGSP_BIC_HP` physics package [15] was used to model the complex interactions of high-energy proton beams, including secondary radiation such as neutrons and photons. This package includes the quark-gluon reactive model, the Bertini cascade approach, and high-precision neutron models [16]. Complementary models, such as `G4Em_Standard_Physics_option4` for electromagnetic processes [17], `G4_Decay_Physics` for particle decay [18], and `G4_Hadron_Elastic_Physics_HP` for elastic scattering of hadrons [19], have also been employed. Additionally, `G4_Ion_Physics` [20] and `G4_Em_Extra_Physics` [21] were used to simulate interactions involving ions and secondary radiation.

To simplify the simulation, particles such as gamma rays (γ), electrons (e^-), positrons (e^+) and neutrinos (ν) were excluded because they do not contribute to the relevant imaging information.

[22] Numerical values for range cut and step limit were selected in order to ensure sufficient level of precision for the simulated data, while optimizing computational resources. Range cut parameter limits the energy level, until which the particle is tracked, and was set to 0.5

mm. Step limit imposes the maximum length a particle can travel without interacting with the surrounding environment and was set to 1 mm.

3. Beam Configuration and Energy Settings

The proton beam initial direction was defined to reflect realistic conditions. Beam-direction vectors were generated in spherical coordinates using the `G4RandFlat` and `G4RandGauss` methods. The polar angle θ was uniformly distributed over 0 to 2π to cover all directions. The azimuthal angle ϕ followed a Gaussian distribution with a mean of 0 and a standard deviation [23] of 3 mrad, representing the typical beam divergence values achieved by accelerators in proton therapy (PT). This captures the realistic angular variations present in clinical proton beams.

The proton beam energy was set with an additional energy spread introduced to reflect the design momentum spread of NIMMS HeLICS design. This spread followed a normal distribution with a [24]standard deviation of 0.2%. The values of standard deviation is based on the [7]NIMMS HeLICS design design momentum spread of 0.1%.

4. Data Acquisition and Output

During the simulations, data were collected at both the incoming and outgoing detector volumes. To provide the inputs necessary for MLP algorithm, following parameters were systematically recorded:

- *Position (X and Y):* Particle coordinates at the entry and exit points.
- *Trajectory Angles (ThetaX and ThetaY):* Angles of motion at entry and exit.
- *Kinetic Energy:* Energy at entry and exit points.
- *Time:* Global time at specific points.
- *Particle ID:* Unique identification of each particle.

5. *Detector and Target Geometry*

After analyzing the simulation data, the focus was shifted to modelling the detector and target geometries. The G4Box class is used to define the cubic structures required for the simulation. The world volume was designed to be large enough to contain all sub-volumes and particles, preventing data loss or unintended interactions.

A Check Volume was placed between the detector and the world volume to identify potential errors or particle leaks. An idealized detector volume was positioned both before and behind the target volume to measure the properties of particles.

The target volume used in the simulation was filled with water to serve as the medium for the travel of the particles.

C. WEPL and Scattering Calculations

1. *Water Equivalent Path Length (WEPL) Calculation*

[10]The WEPL plays a key role both in proton beam therapy and radiography applications. It is calculated as the integral of the path of the RSP or the path length in water, which accounts for the observed proton energy loss. WEPL lookup tables in water were calculated using the Bethe-Bloch equation [25](Equation 1), which describes the energy loss of charged particles, such as protons, as they interact with matter.

The Bethe-Bloch equation is expressed as follows:

$$\frac{dE}{dx} = \frac{KZ^2}{\beta^2} \left(\frac{1}{2} \ln \frac{2m_e c^2 \beta^2 \gamma^2 T_{\max}}{I^2} - \beta^2 \right) \rho \tag{1}$$

where:

- $\frac{dE}{dx}$: energy loss per unit length,
- K: constant representing $0.307\,\mathrm{MeV\ cm^2/g}$,
- Z: proton charge,
- β: relative proton velocity,
- γ: Lorentz factor,

- $T_{\max}$: maximum kinetic energy a proton can transfer to an electron,

- I: average ionic potential of water (78 eV),

- ρ: material density.

Lookup tables are used in image reconstruction process to convert the kinetic energy of exiting particles into WEPL values. The WEPL was calculated iteratively, simulating energy losses in [26]small path length increments (0.01 cm).

2. Momentum-Velocity Calculations

In addition to WEPL, the momentum-to-velocity functions ($\frac{p}{\beta}$) were calculated for the necessary parameters for MLP reconstruction algorithm. These functions are then used for particle scattering estimations due to MCS, ensuring the accuracy for proton path reconstruction for imaging analysis. This ratio is calculated using the following [27]relativistic Equation (2):

$$\frac{p}{\beta} = \frac{E + m_p c^2}{c \cdot \beta} \tag{2}$$

where:

- p is the momentum,

- β is the ratio of the particle velocity to the speed of light,

- E is the kinetic energy of the proton,

- m_p is the proton's rest mass,

- c is the speed of light.

Polynomial approximations were used to describe the momentum-velocity relationship at various energy levels (250, 330, 400, 500, 600, and 700 MeV) and depths (16 and 32 cm), to ensure efficiency in furthe calculations. The polynomial is expressed by [28] Equation (3) as follows:

$$P(x) = a_5 x^5 + a_4 x^4 + a_3 x^3 + a_2 x^2 + a_1 x + a_0 \tag{3}$$

where x represents the depth (cm) and $a_0, a_1, \ldots, a_5$ are the polynomial coefficients determined by fitting calculated values using the least squares methods. The percentage difference between the polynomial model and original data was calculated to verify the quality of the approximation.

3. *Modelling Multiple Coulomb Scattering (MCS)*

[4]Unlike X-rays, protons undergo multiple small-angle scattering as they pass through an object, causing deviations from their original path and potential image blurring, particularly if they are not captured immediately behind the object. Even with optimal positioning, some blurring still occurs due to scattering effects.

To account for the effects of multiple scattering on proton trajectories for MLP algorithm, we applied [28]R.W. Schulte's formalism, which uses a Bayesian statistical approach and assumes the Gaussian approximation of MCS. This method predicts proton paths by incorporating the entry and exit positions and angular directions. Schulte's approach is valued for its balance between precision and computational efficiency, making it well suited for MLP algorithm.

4. *Scattering Matrices*

Schulte's approach employs a Gaussian approximation within the MCS framework based on the generalized [29]Fermi-Eiges theory. This approach allows to estimate the proton path as it traverses different materials, accounting for both the continuous energy loss and scattering. The trajectory of a proton crossing an object was calculated by defining the U-axis as the main proton path orthogonal to the detector plane, whereas the t and v planes remained parallel to the detector plane. The depth u_1 and its corresponding vertical coordinates v_1, along with the angles θ_1 and ϕ_1, were used to describe the lateral and vertical scattering of the proton. The position of the proton at any given depth can then be represented by a two-dimensional vector $\mathbf{y}_1$ for the entry and $\mathbf{y}_2$ for the exit, as shown in [28]Equation 4:

$$\mathbf{y}_1 = \begin{pmatrix} t_1 \\ \theta_1 \end{pmatrix} \quad \text{and} \quad \mathbf{y}_2 = \begin{pmatrix} t_2 \\ \theta_2 \end{pmatrix} \tag{4}$$

To predict the proton trajectories within this framework, it is necessary to accurately quantify the scattering processes that contribute to these paths. [28]Equations 5–7 define the variances and covariances of the lateral displacement t_1 and angle θ_1 formed along the proton path between the depth points u_0 and u_1. At this stage, the motion of the proton is characterized by its initial momentum, dispersion, and energy loss, which gradually decrease with increasing depth.

$$\sigma_{t_1}^2(u_0, u_1) = E_0^2 \left[1 + 0.038 \ln\left(\frac{u_1 - u_0}{X_0}\right)\right] \int_{u_0}^{u_1} \frac{(u_1 - u)^2}{\beta^2(u)p^2(u)} \frac{du}{X_0}, \tag{5}$$

$$\sigma_{\theta_1}^2(u_0, u_1) = E_0^2 \left[1 + 0.038 \ln\left(\frac{u_1 - u_0}{X_0}\right)\right] \int_{u_0}^{u_1} \frac{1}{\beta^2(u)p^2(u)} \frac{du}{X_0}, \tag{6}$$

$$\sigma_{t_1\theta_1}^2(u_0, u_1) = E_0^2 \left[1 + 0.038 \ln\left(\frac{u_1 - u_0}{X_0}\right)\right] \int_{u_0}^{u_1} \frac{(u_1 - u)}{\beta^2(u)p^2(u)} \frac{du}{X_0}. \tag{7}$$

On the other hand, Equations [28]8–10 are analogous to Equations (5-7), but describe the dispersion and covariance of the lateral displacement t_2 and angle θ_2 during the second stage of the proton path, between the depth points u_1 and u_2. At this stage, the proton continues to lose energy, and its trajectory shifts. These changes were calculated based on the initial variance and covariance values, along with additional scattering events that occurred within this depth range.

$$\sigma_{t_2}^2(u_1, u_2) = E_0^2 \left[1 + 0.038 \ln\left(\frac{u_2 - u_1}{X_0}\right)\right] \int_{u_1}^{u_2} \frac{(u_2 - u)^2}{\beta^2(u)p^2(u)} \frac{du}{X_0}, \tag{8}$$

$$\sigma_{\theta_2}^2(u_1, u_2) = E_0^2 \left[1 + 0.038 \ln\left(\frac{u_2 - u_1}{X_0}\right)\right] \int_{u_1}^{u_2} \frac{1}{\beta^2(u)p^2(u)} \frac{du}{X_0}, \tag{9}$$

$$\sigma_{t_2\theta_2}^2(u_1, u_2) = E_0^2 \left[1 + 0.038 \ln\left(\frac{u_2 - u_1}{X_0}\right)\right] \int_{u_1}^{u_2} \frac{(u_2 - u)}{\beta^2(u)p^2(u)} \frac{du}{X_0}. \tag{10}$$

Where, $\beta(u)$ and $p(u)$ represent the squared velocity with respect to the speed of light and the momentum of the proton at depth u, respectively, $E_0 = 13.5\,\mathrm{MeV}/c$ is an empirical parameter introduced by [30]Leach and Dahl that characterizes the effect of scattering, and

X_0 is the length of the radiation, which is a constant for a particular material. Here we assume that the scattering object consists of water, for which $X_0 = 36.1\,\text{cm}$.

Having established the variances and covariances for the lateral displacement (t_1, t_2) and angle (θ_1, θ_2) at different stages of the proton trajectory, these values are organized into scattering matrices that can be used to calculate the position of proton and velocity direction as it progresses through the medium.

The scattering matrices Σ_1 and Σ_2 [28](Equations 11, 12) encapsulate the statistical relationships between the lateral displacement and angular deviations at specific depth points, u_0, u_1, and u_2. Σ_1 corresponds to the scattering parameters between the points u_0 and u_1, while Σ_2 represents the scattering characteristics between u_1 and u_2 as the proton continues its path through the medium.

The structure of these matrices is given by:

$$\Sigma_1 = \begin{pmatrix} \sigma_{t_1}^2 & \sigma_{t_1\theta_1} \\ \sigma_{t_1\theta_1} & \sigma_{\theta_1}^2 \end{pmatrix} \tag{11}$$

$$\Sigma_2 = \begin{pmatrix} \sigma_{t_2}^2 & \sigma_{t_2\theta_2} \\ \sigma_{t_2\theta_2} & \sigma_{\theta_2}^2 \end{pmatrix} \tag{12}$$

These matrices describe the variance and covariance of the lateral displacement and angular deviation of the proton at different points along the path. Σ_1 captures scattering at the beginning of the trajectory, whereas Σ_2 represents the scattering as the proton approaches the end of its path.

5. *Geometric Matrices*

After defining the scattering matrices, the next step involves the geometric matrices, which transform the spatial coordinates of the protons as they move through different depths. The matrices R_0 and R_1 [28](Equations 13, 14) describe the positional and angular relationships at intervals defined by depth points u_0, u_1, and u_2. In the 16-cm phantom, these depth points were set to $u_0 = 0\,\text{cm}$, $u_1 = 8\,\text{cm}$, and $u_2 = 16\,\text{cm}$. For the 32 cm phantom, $u_0 = 0\,\text{cm}$, $u_1 = 16\,\text{cm}$, and $u_2 = 32\,\text{cm}$.

The matrix R_0 represents the transition from the initial depth u_0 to the intermediate depth u_1, adjusting the trajectory of the proton based on its entry angle θ_0, which is generally small for proton beams. Matrix R_1 captures the transition from u_1 to the final depth u_2, accounting for the proton's lateral displacement and scattering angle as it approaches the end of its path. The structures of the matrices are as follows:

$$R_0 = \begin{pmatrix} 1 & u_1 - u_0 \\ 0 & 1 \end{pmatrix} \tag{13}$$

$$R_1 = \begin{pmatrix} 1 & u_2 - u_1 \\ 0 & 1 \end{pmatrix} \tag{14}$$

The scattering matrices (Σ_1, Σ_2) and geometric matrices (R_0, R_1) together provide the foundation for predicting the most likely path of the proton, as well - the associated uncertainty of the trajectory. In the next sections, the full MLP formalism is explained in detail for the image-reconstruction process.

D. Data filtration

As protons pass through material, various physical interactions mechanisms are of relevance. In the case of the proton radiography and assumptions made for the image reconstruction process, presence of particles that have underwent specific processes such as inelastic scattering or large-angle MCS, could influence the quality of the reconstructed image. In order to reduce such artifacts, various data filters should be applied for the full set. These algorithms were developed using [31]Python version 3.12 to aid this analysis.

1. *General Filtration Methods*

Energy filtering was applied to remove anomalous values that could have distorted the analysis. [32]Data points outside the $[\text{mean} - 3\sigma; \text{mean} + 3\sigma]$ range were excluded, retaining only protons with energy losses consistent with expected material properties.

Second, relative angle filtering was applied to focus on the primary proton trajectories, thereby reducing the scattering effects. Similar to energy filtering, this method uses a Gaussian distribution to exclude angular data outside the $[\text{mean} - 3\sigma; \text{mean} + 3\sigma]$ range for both the X and Y components.

Additionally, a "1-to-1" filtration ensures that each input particle corresponds to one output particle, eliminating secondary particles and noise. A marker value was used in the data set to differentiate output data points corresponding to specific input data points.

For the simple geometry used for spatial resolution estimation, energy filter was implemented using a double Gaussian fit to assess its effectiveness. Figure 3 shows the filtered energy distribution at 250 MeV and 16 cm depth, where two Gaussian peaks are present, corresponding to protons passing through water and high-contrast medium. The application of 3σ boundaries successfully excluded outliers and preserved only protons with consistent energy losses for further analysis.

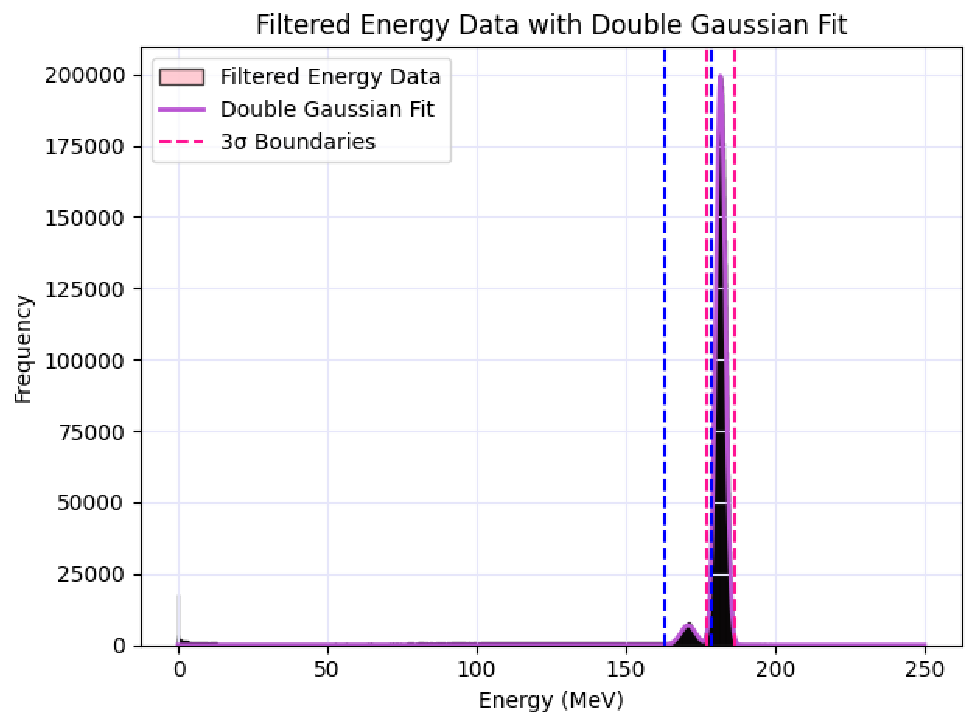

FIG. 3: Filtered Energy Data with Double Gaussian Fit at 250 MeV and 16 cm Depth. This figure illustrates the energy distribution of protons after filtration at 250 MeV and a depth of 16 cm. The primary Gaussian peak, corresponding to the main proton population, showed minimal scattering, with outliers removed using the 3σ filtering method. The fit revealed a clear energy distribution, indicating the effectiveness of the filtration process in maintaining data consistency for further analysis.

In contrast, Figure 4 shows the energy distribution at 250 MeV but at a depth of 32 cm. Here, a more complex double Gaussian distribution appears, reflecting the increased scattering and interactions at greater depths. This resulted in "smearing out" of the two distinct energy peaks, demonstrating the challenges in maintaining stable proton trajectory reconstruction in thicker geometries.

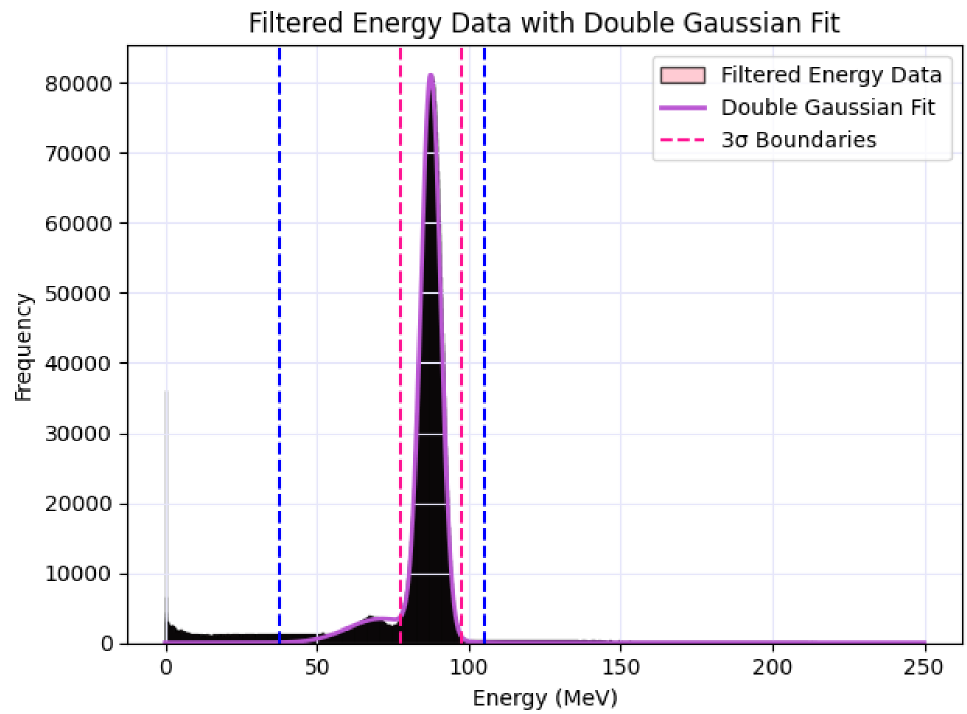

FIG. 4: Filtered Energy Data with Double Gaussian Fit at 250 MeV and 32 cm Depth. This figure presents the energy distribution of the protons at 250 MeV and a depth of 32 cm after applying the filtration process. The double Gaussian fit highlights increased scattering at this depth, with two distinct peaks reflecting more complex proton interactions within the phantom. The use of 3σ filtering effectively reduced outliers, ensuring that only protons with consistent energy losses were included for further analysis.

2. *Pixel-wise Energy Filtering*

[33]Pixel-wise filtering, a sub-method of energy filtering, was used to refine the dataset, particularly in complex geometries where standard energy filtering with a Gaussian fit may not suffice. While Gaussian fitting is effective for simpler geometries, pixel-wise filtering provides a more precise approach for intricate structures in clinically relevant proton imaging.

Accurate contrast resolution in proton imaging depends on the precise measurement of the WEPL values across individual pixels. Given the variations in material density and composition, significant discrepancies in the expected WEPL values can occur between pixels.

To address these complexities, the pixel-wise filtering process began by pre-categorizing the raw data according to the X and Y positions calculated at the reconstruction depth, assuming straight trajectory between entrance and exit point. This binning allowed for a more granular analysis of the proton energy at each pixel, ensuring that the reconstruction process accounted for localized proton interactions as they traversed the medium.

Subsequent energy filtering involves assigning a mode energy value to each pixel, representing the most frequent energy occurrence. [34]A margin of 25% around this mode value was applied for initial filtering. Finally, the 3σ criterion was used to exclude any values outside the bounds of a normal distribution, ensuring that only the most representative data points were retained. For this, mean and standard deviations was calculated for the data array of each pixel.

III. IMAGE RECONSTRUCTION USING THE MOST LIKELY PATH (MLP) FORMALISM

A. MLP Formalism Overview

[10]In PT, assuming a straight-line path for protons results in poor spatial resolution because of MCS as protons pass through a medium. To address this limitation, MLP formalism is typically used. This probabilistic model reconstructs curved proton trajectories while accounting for scattering effects, thereby improving the spatial resolution and enabling more accurate image reconstruction.

The MLP formalism used in this study is based on the matrix-based approach proposed by [28]Schulte et al., which builds on the methods of Williams and the [29]Fermi-Eyges framework. By applying Bayesian techniques to a bivariate Gaussian distribution, the MLP model calculates the most likely lateral position and angular deflection of a proton at a certain depth, given its entry and exit conditions. This model plays a key role in predicting proton trajectories and serves as a foundation for high-resolution PR.

B. MLP Calculation Framework

The MLP formalism relies on both scattering and geometric matrices, which describe the state of a proton at different points along its path. The scattering matrices Σ_1 and Σ_2, along with geometric matrices R_0 and R_1, are derived in Section 2.4. These matrices, combined with the initial and final state vectors $\mathbf{y}_0$ (entry) and $\mathbf{y}_2$ (exit), provide inputs for calculating the MLP. The final MLP [28]Equation(III B) used for reconstruction can be expressed as:

$$\mathbf{y}_{\mathrm{MLP}} = \left(\Sigma_1^{-1} + R_1^T \Sigma_2^{-1} R_1\right)^{-1} \left(\Sigma_1^{-1} R_0 \mathbf{y}_0 + R_1^T \Sigma_2^{-1} \mathbf{y}_2\right) \tag{15}$$

In this formula:

- R_0 and R_1 are geometric matrices that account for position and angle transformations, respectively.
- Σ_1 and Σ_2 are scattering matrices that represent uncertainties in the position and angle, respectively.
- $\mathbf{y}_0$ and $\mathbf{y}_2$ are the proton entry and exit vectors, respectively.

This equation incorporates the MCS effects and offers a reliable method for predicting the most likely proton path through the medium. [10]Figure 5 presents a schematic of the particle imaging system, illustrating how the MLP formalism is used to estimate the proton's trajectory as it traverses the medium.

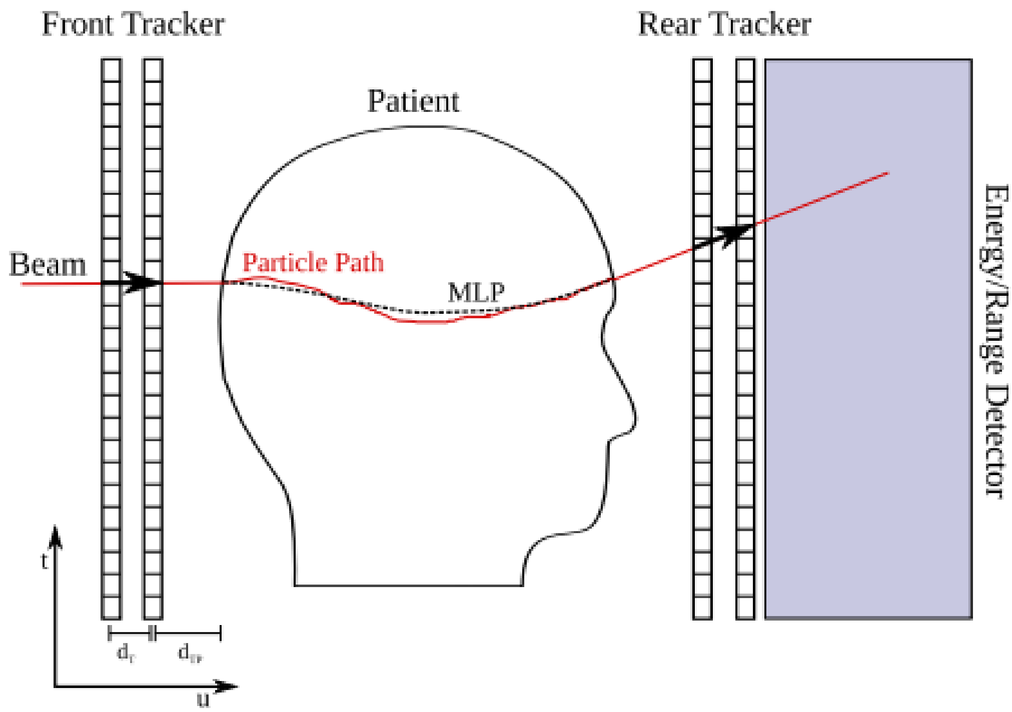

FIG. 5: This diagram illustrates the application of the MLP formalism in proton therapy. The red curve shows the actual proton path through a water-equivalent phantom (the patient is shown for illustrative purposes only). The dotted black line represents the MLP, which estimates the proton's most likely path, considering the scattering effects. Measurements were made at the front and rear trackers, with the residual energy of the proton measured using an energy/range detector. The positional and angular data at the entry and exit points, along with the WEPL values, were used to accurately reconstruct the trajectory of the proton.

C. Pixel Binning and WEPL Calculation

[35]Following the MLP trajectory calculations, proton data were binned into pixels for image reconstruction, using a resolution of 0.2 mm per pixel to ensure high spatial detail. The trajectory of each proton from entry to exit was traced, and MLP-derived lateral positions were used to assign protons to the appropriate pixel bins.

For each pixel, WEPL was calculated based on corresponding average kinetic energy of exiting particles after binning, by interpolating the pre-calculated lookup data.

IV. IMAGE ANALYSIS

A. MTF (Modulation Transfer Function) Analysis

[10]The Modulation Transfer Function (MTF) is a key metric for evaluating the spatial resolution of imaging systems. It quantifies the system's ability to preserve detail and contrast, and provides valuable insights into the performance of the image reconstruction process. In this study, the MTF was calculated using an aluminum cube located at the center of the phantom as the reference object.

The MTF calculation begins by extracting the central intensity profile from the reconstructed image, which represents the signal intensity distribution across the aluminum cube and surrounding regions. This profile was taken along both the horizontal and vertical axes, and then averaged and filtered to reduce noise, ensuring accurate analysis of the spatial resolution.

Next, the [10]Line Spread Function (LSF) was derived by numerically differentiating the averaged central profile. To refine the LSF, a Gaussian function was fitted to the differentiated data, smoothing the LSF and reducing noise and outliers for a more accurate calculation.

The MTF was obtained by applying a Fourier transform to the Gaussian-fitted LSF, and converting the spatial domain data into the frequency domain. This reveals the efficiency of the system in transmitting different spatial frequencies corresponding to the various levels of geometrical detail. The MTF curve was analyzed to determine the spatial frequencies at which the MTF values decreased to [36]50% and [37]10% of their maximum. These thresholds are key indicators of the system's spatial resolution, with the 50% value typically representing the system's limiting resolution.

Figure 6 show central intensity profiles along the horizontal and vertical axes through the aluminum The red lines represent the averaged profiles, with the central region indicating the region of the highest intensity at the edge of the cube.

B. Contrast-to-Noise Ratio (CNR) Evaluation

While MTF offers insights into spatial resolution and detail preservation, it is also necessary to assess the system's ability to distinguish between different materials or regions within

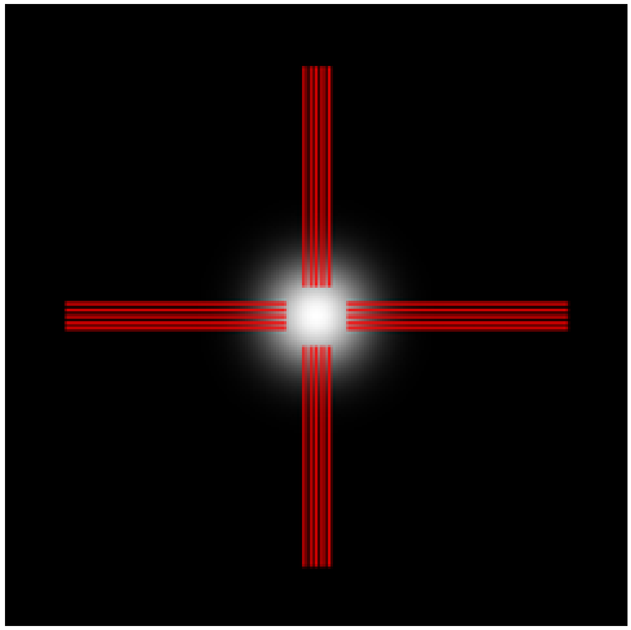

FIG. 6: Visualization of the Modulation Transfer Function (MTF) Calculation Process. This figure depicts the process of calculating LSF for further analysis of the Modulation Transfer Function (MTF). The MTF quantifies a system's ability to resolve different spatial frequencies.

an image. This is quantified by the [10]Contrast-to-Noise Ratio (CNR), which complements spatial resolution analysis by focusing on the contrast performance. In this study, the CNR was calculated using [10]Equation 16 to evaluate the contrast between the aluminum cube embedded in the water-equivalent phantom and its surrounding background.

The CNR is mathematically expressed as:

$$\mathrm{CNR} = \frac{\mathrm{WEPL}_{\mathrm{AlCube}} - \mathrm{WEPL}_{\mathrm{water}}}{\sqrt{\sigma^2_{\mathrm{AlCube}} + \sigma^2_{\mathrm{Water}}}} \tag{16}$$

where $\mathrm{WEPL}_{\mathrm{AlCube}}$ and $\sigma^2_{\mathrm{AlCube}}$ represent the mean and standard deviation, respectively, of the WEPL values in the central area of the aluminium region, and $\mathrm{WEPL}_{\mathrm{water}}$ and $\sigma^2_{\mathrm{Water}}$ are the mean and standard deviation of the WEPL values in the surrounding water-equivalent region.

In imaging systems, signal intensity is related to the number of detected particles or their energy deposition within the detector medium. The mean WEPL value in a region represents the average energy deposited by incident particles. In this study, $\mathrm{WEPL}_{\mathrm{AlCube}}$ corresponds to the energy deposition within the aluminum cube, whereas $\mathrm{WEPL}_{\mathrm{Water}}$ reflects deposition in the surrounding water-equivalent background.

The standard deviation σ represents the system noise, which can result from factors such as quantum noise, electronic noise, and material properties. A higher σ indicates greater signal variability, making it more difficult to distinguish between regions with different mean WEPL values.

To calculate the CNR, the study focused on a specific region from $-50\,\text{mm}$ to $50\,\text{mm}$ along both axes. The aluminum region was defined from $-5\,\text{mm}$ to $5\,\text{mm}$ and was centrally located in the phantom. The mean WEPL ($\text{WEPL}_{\text{AlCube}}$) and standard deviation (σ_{AlCube}) for this region were calculated, excluding background contributions.

The background region was selected diagonally opposite the aluminum cube to avoid influence of scattering. The mean WEPL ($\text{WEPL}_{\text{Water}}$) and standard deviation (σ_{Water}) for this region were computed in a similar manner.

C. Dose calculations

[38]The absorbed dose, measured in Gray (Gy), quantifies the amount of energy deposited by ionizing radiation in a given mass of material. In this study, the absorbed dose was calculated using [38]Equation 17 to evaluate the energy deposition resulting from the proton interactions.

The absorbed dose is defined as:

$$\text{Dose (Gy)} = \frac{\text{Total Energy Deposited (J)}}{\text{Mass (kg)}} \tag{17}$$

where the total deposited energy is the sum of the kinetic energy transferred from the incident particles to the medium. The conversion from MeV to Joules was performed using the conversion factor $1\,\text{MeV} = 1.60218 \times 10^{-13}\,\text{J}$.

In this study, the total energy deposited in the phantom was obtained by summing the energy values from the simulation output (MeV), which were then used to calculate the absorbed dose, factoring in the specific mass of the phantom material.

D. Comparison Between Theoretical and Experimental Images

To assess the accuracy of the imaging system, a quantitative analysis was performed by comparing the theoretically predicted images with experimentally obtained images within MC simulations. This analysis focused on two key scenarios: an aluminum cube at different depths within the phantom, and a low-contrast phantom with cylindrical geometries simulating various human tissue types.

The theoretical images were generated with a [24]0.2 mm resolution, using pre-calculated WEPL values for both the aluminum cube and the low-contrast phantom at depths of 16 cm and 32 cm, consistent with the experimental setup. These predictions are based on the expected material interactions at these depths.

The comparison involved evaluating the absolute difference, quantifying the direct discrepancy between the experimental and theoretical WEPL values, and calculating the percentage difference, expressing the deviation relative to the theoretical values. These differences were visualized as "difference images," providing a quantitative measure of the system's performance against theoretical predictions.

V. RESULTS - ANALYSIS OF THE SIMULATION RESULTS

A. Spatial Resolution dependence on the energy and phantom thickness

1. MTF 50% and MTF 10%

This section focuses on the analysis of achievable spatial resolution within proton radiography at the different energy levels and phantom thicknesses studied. The results for a thickness of 16 cm show a consistent increase in the MTF values as the proton beam energy increases from 250 to 700 MeV. Specifically, the 50% MTF values started at 0.0245 cycles/mm at 250 MeV and increased to 0.1364 cycles/mm at 700 MeV, indicating a significant improvement in the system's ability to resolve finer details, reflecting the superior spatial resolution at higher energies. Similarly, the MTF 10% values, which represent the sensitivity of the system to textural nuances, increased from 0.488 to 0.697 cycles/mm. This improvement in texture detection highlights the system's enhanced capability to resolve smaller structures as energy increases, owing to reduced beam lateral spread.

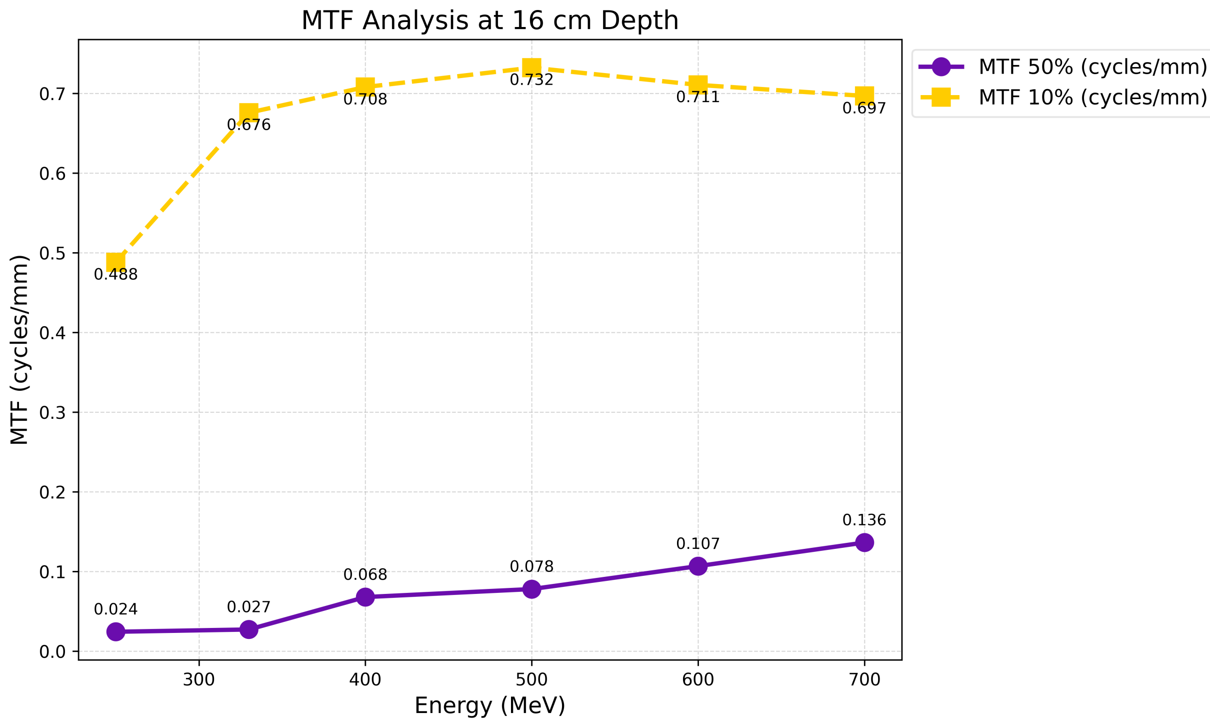

FIG. 7: MTF Analysis for a thickness of 16 cm. This figure displays the Modulation Transfer Function (MTF) values at both the 50% and 10% thresholds across a range of proton beam energies (250–700 MeV). The graph highlights how the spatial resolution improves with increasing energy, reflecting the system's capacity to resolve fine details at different proton beam energies for a thickness of 16 cm.

For a thickness of 32 cm, the modulation transfer function data showed a distinct peak at 600 MeV, where the MTF 50% values reached 0.298 cycles/mm. Following this, there was a slight decline in the resolution, with MTF 50% values dropping to 0.266 cycles/mm at 700 MeV. This reduction suggests possible limitations due to changes in nuclear interaction rates, which can potentially degrade image quality at higher energies. Similarly, the MTF 10% values peaked at 0.272 cycles/mm at 600 MeV before decreasing slightly. This pattern, suggests the balance between energy and depth, showing that while higher energies improve penetration, they may not always enhance resolution because of the complexities of the beam-tissue interactions Figure 8.

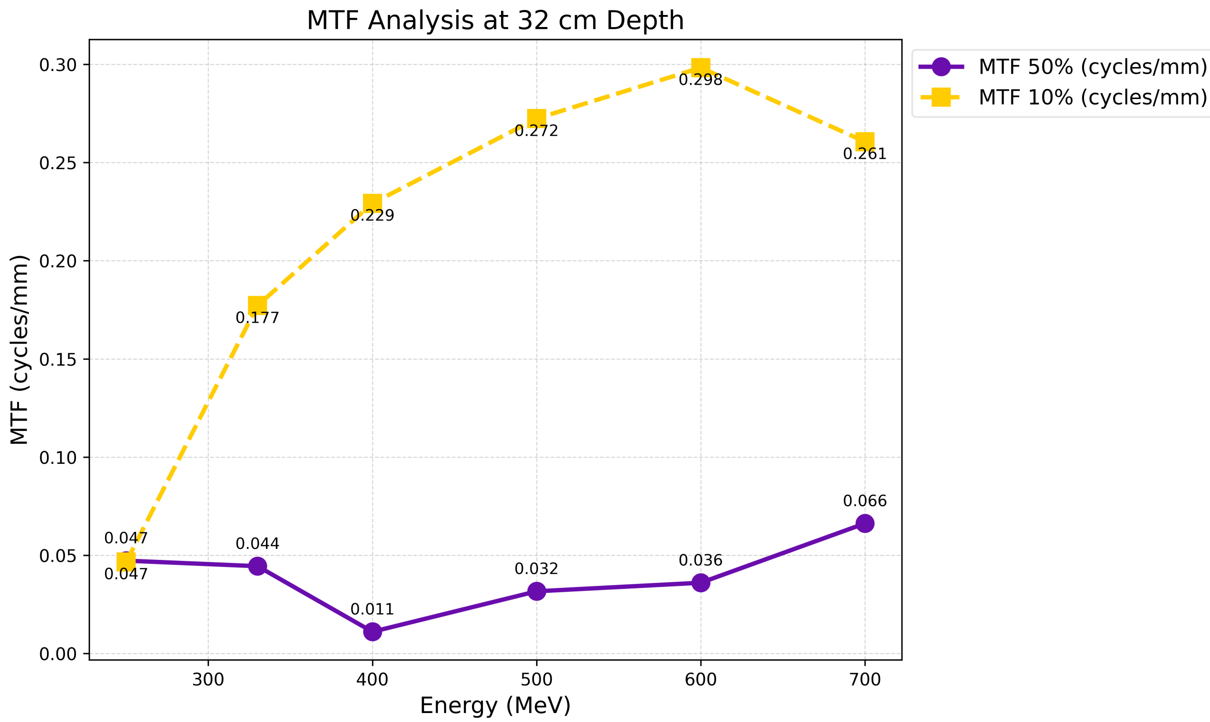

FIG. 8: MTF Analysis for a thickness of 32 cm. This figure presents the Modulation Transfer Function (MTF) values at both the 50% and 10% thresholds across proton beam energies ranging from 250 to 700 MeV. The data illustrate how the spatial resolution changes with energy levels, highlighting the system's performance for a thickness of 32 cm.

For a thickness of 16 cm, increasing the energy to 700 MeV improved the spatial resolution by reducing lateral beam spread, as shown by the steady increase in both MTF 50% and MTF 10% values. In contrast, for a thickness of 32 cm, the resolution peaked at 600 MeV, with higher energies leading to slightly decreased quality owing to possibly increased probability of nuclear interactions. From perspective of spatial resolution performance, the identified optimal energies of 600 and 700 MeV provide the basis for further investigations.

2. *Visual Analysis of Reconstructed Images*

While the MTF analysis quantifies the spatial resolution of the system at different energy levels, further insight is gained by examining the reconstructed images. These images, generated at 250 MeV and 700 MeV for for a thicknesses 16 cm and 32 cm, visually demonstrate the impact of imaging energy on the system's ability to resolve high-contrast objects, such as aluminum cubes. Visual comparison complements the MTF data by providing a clear representation of the spatial resolution performance of the system under various energetic conditions.

At 250 MeV and 16 cm thickness Figure 9, the image shows an aluminum cube, but the edges are blurred, resulting from increased scattering. This blurring is due to MCS, which disperses the proton paths, leading to broader intensity profiles around the object. The lower energy limits the ability of the system to maintain tight proton trajectories and reduce the spatial resolution. The halo effect around the cube highlights the system's difficulty in resolving its boundaries precisely at this energy level. A lower proton energy causes greater deflection angles, which broadens the proton distribution at the detector. Despite these limitations, the contrast between the aluminum cube and surrounding water phantom was sufficient, although the fine detail resolution was compromised.

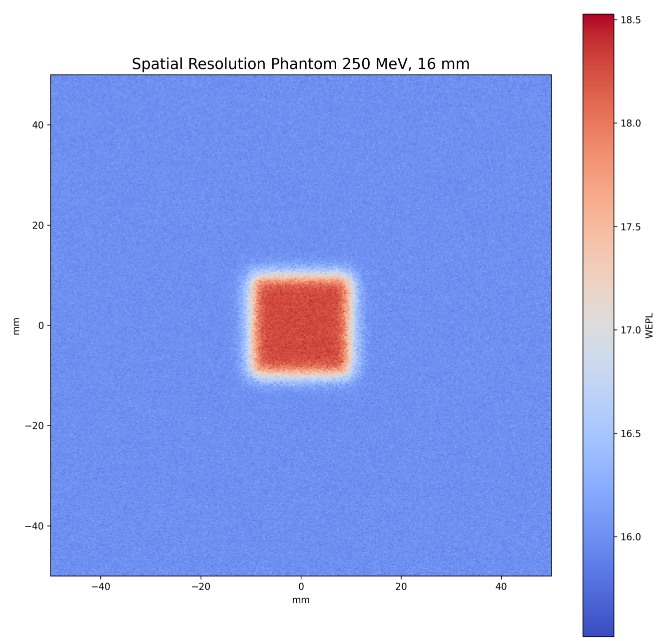

FIG. 9: Reconstructed Image at 250 MeV, 16 cm thickness. This image shows the reconstructed region at 250 MeV with thickness of 16 cm, referring to the placement of an aluminum cube within the water phantom. The spatial dimensions were represented in millimeters (mm), corresponding to the field of view of the reconstructed area.

Following the analysis for a thickness of 16 cm, the spatial resolution was further evaluated for a thickness of 32 cm Figure 10, as shown in the reconstructed image at 250 MeV. At this depth, the extended proton path through the medium resulted in more pronounced scattering effects. This leads to significant blurring, with the edges of the aluminum cube appearing heavily diffused and less distinguishable compared with the 16 cm thickness.

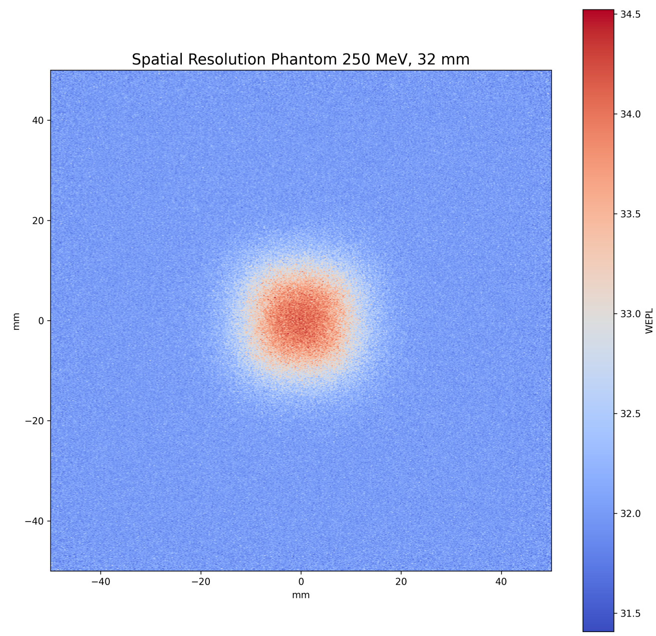

FIG. 10: Reconstructed Image at 250 MeV, 32 cm thickness

The central region of the cube retains some contrast relative to the surrounding phantom; however, the lack of a clear edge definition highlights the limitations of low-energy protons at this depth. The spread of proton paths results in a broader, more uniform distribution of energy, reduced spatial resolution, and diminished ability to resolve fine structural details.

The halo effect observed in the image indicates that many protons underwent significant angular deflection, contributing to the wide intensity distribution.

Overall, the image suggests that at 250 MeV, the energy is insufficient to produce a clear, high-resolution image because the system's ability to accurately reconstruct the object is compromised.

In contrast, the spatial resolution at 700 MeV for the 16 cm thickness in Figure 11 shows a significant improvement compared with the 250 MeV images. At this higher energy, proton beams achieve greater penetration and less lateral dispersion owing to their higher momentum and reduced deflection by the atomic nuclei. The reconstructed image reflects this, with sharply defined cube edges and a minimized halo effect.

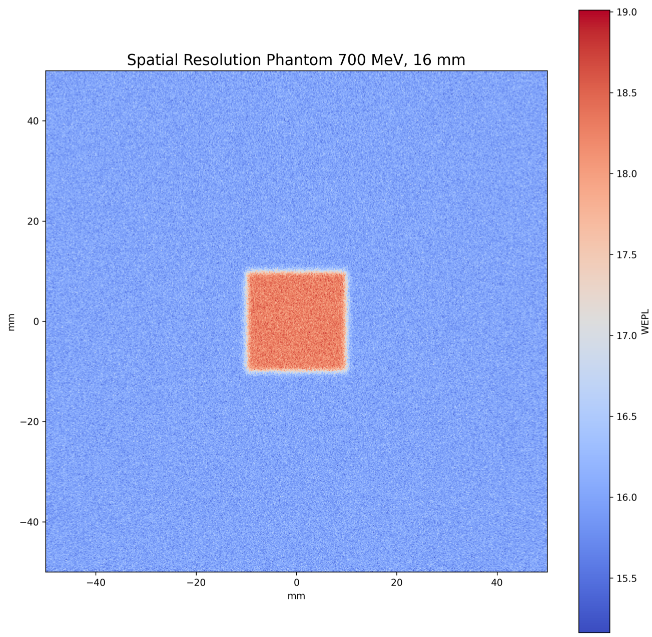

FIG. 11: Reconstructed Image at 700 MeV, 16 cm thickness

At 700 MeV, the protons followed a more direct path through the water phantom, due to significantly reduced lateral scatterin. This significantly enhances the system's ability to capture fine structural details. The aluminum cube was clearly resolved, with a well-preserved contrast between the cube and the surrounding medium. This demonstrates the capability of the system to utilize high-energy protons to minimize blurring and achieve higher spatial resolution.

For a thickness of 32 cm, the 700 MeV reconstructed image in Figure 12 shows a reduced resolution compared to the 16 cm thickness, despite the higher energy. Although the increased energy allows deeper penetration, scattering becomes more pronounced at this extended depth, resulting in a noticeable loss of edge definition, with the aluminum cube appearing blurred and less distinct from the surrounding water phantom.

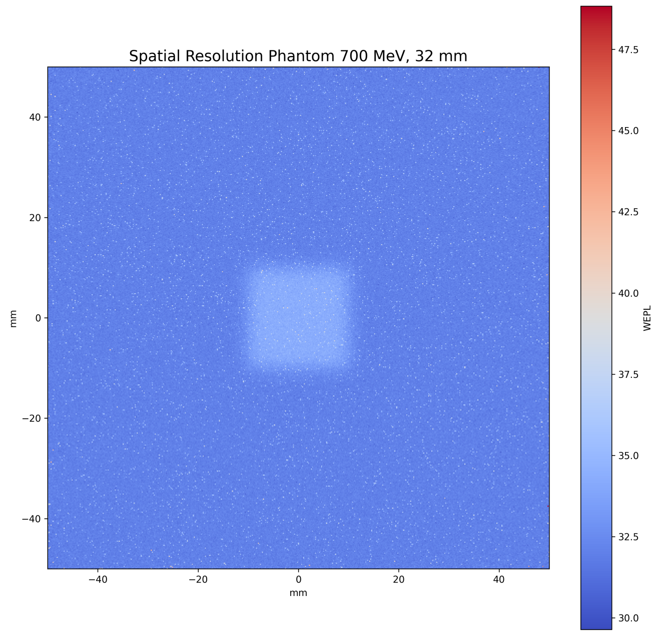

FIG. 12: Reconstructed Image at 700 MeV, 32 cm thickness

The combination of depth and scattering resulted in a more diffuse intensity distribution. Although a higher energy reduces some scattering effects, the cumulative interactions over a longer path in the phantom degrade the spatial resolution. Even at 700 MeV, where proton trajectories are better maintained, substantial deflection still occurs, limiting the system's ability to accurately reconstruct fine details. Although the spatial resolution is clearly reduced, performance of 700 MeV is visually significantly better compared to 250 MeV.

3. Difference Image Analysis

Further insights into the impact of proton energy and thickness of the phantom on image quality can be gained by examining difference images - comparison of simulated radiographs with theoretically calculated ones. These images highlight variations in WEPL reconstruction accuracy, edge definition, and blurring owing to lateral scattering, allowing for a clear comparison between the energy levels. The absolute difference image at 250 MeV and 16 cm thickness in Figure 13 offers a clear visualization of the discrepancies between the theoretically calculated and experimentally reconstructed simulated image.

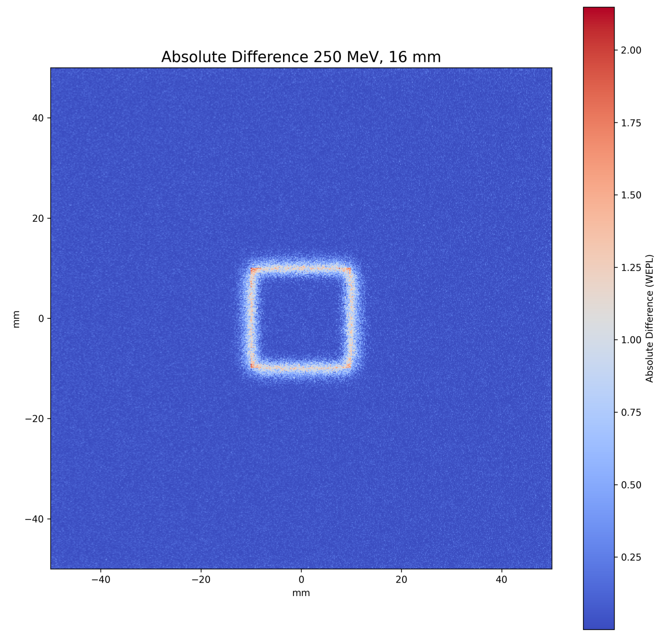

FIG. 13: Absolute Difference Image at 250 MeV, 16 cm thickness.The absolute difference values represent pixel-wise discrepancies between the theoretical and reconstructed images in Water Equivalent Path Length (WEPL). The color scale highlights these differences, with darker areas indicating smaller deviations and lighter areas showing larger discrepancies, particularly around object boundaries.

The most significant deviations were observed along the edges of the aluminum cubes, highlighting the system's limitations in resolving the sharp edges at this energy level. These differences indicate that the reconstruction algorithms do not fully account for the lateral spread of protons at different material interfaces, leading to boundary blurring. In contrast, the central regions of the cube show minimal variation, suggesting the accurate reconstruction of larger features within homogeneous regions.

Most pixels exhibited small absolute differences, indicating that the experimental reconstruction closely aligned with the theoretical model in most areas. The localized discrepancies at the borders suggest a high overall resolution with errors confined to regions of greater proton-path uncertainty due to material interfaces.

In the absolute difference image at 250 MeV and a thickness of 32 cm Figure 14, it is evident that as the thickness increases, proton scattering and image degradation becomes more pronounced. As with the 16 cm thickness, the largest differences were localized around the edges of the aluminum cube, but these deviations were more severe at greater depths because of the cumulative scattering effects over the longer path. This increased diffusion led to greater blurring and reduced resolution at the boundaries of the cube.

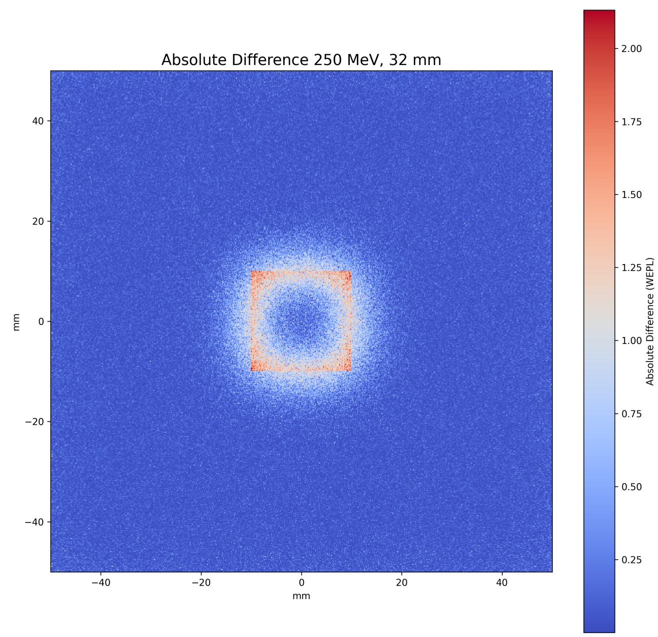

FIG. 14: Absolute Difference Image at 250 MeV, 32 cm thickness

The central regions, while still relatively consistent with the theoretical model, showed slightly more deviation compared to the 16 cm thickness, highlighting the difficulty of maintaining image clarity at greater depths. Although most pixels still exhibit small differences, the number of outliers, particularly around the periphery, increased, underscoring the challenge of preserving the image quality at this depth.

The absolute difference image at 700 MeV and 16 cm thickness in Figure 15 illustrates how higher energy levels improve the system's ability to resolve spatial details. At 700 MeV, reduced scattering and greater penetration resulted in improved spatial resolution compared with lower energy levels. The most notable improvement is the reduction in absolute differences along the edges of the aluminum cube, as higher-energy protons experience minimal lateral deflection, leading to sharper boundary resolution even at material interfaces.

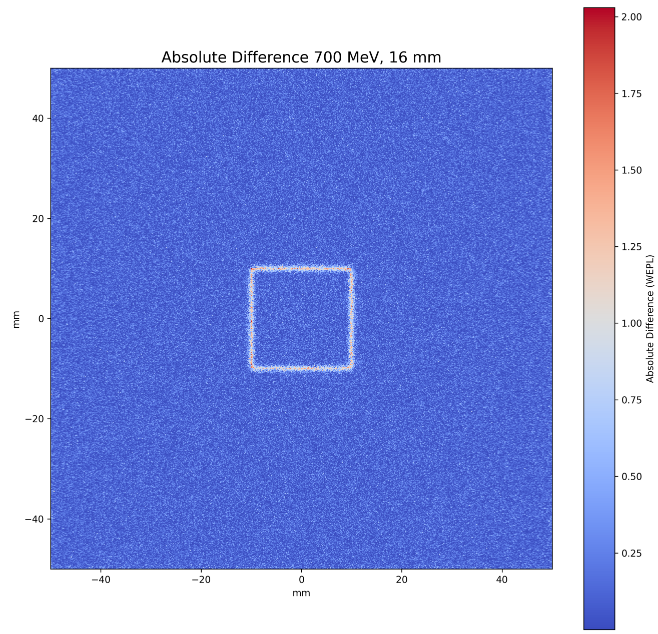

FIG. 15: Absolute Difference Image at 700 MeV, 16 cm thickness

In the central regions of the cube, the absolute differences are even smaller, as high-energy protons maintain straighter paths owing to the reduced scattering. This allows for a more accurate reproduction of the core of the cube, as seen in the smaller difference values concentrated in these regions. Some minor deviations remained at the cube boundaries, but they were significantly reduced compared to those at lower energies.

The absolute difference image at 700 MeV and 32 cm thickness in Figure 16 highlights the spatial resolution performance of the system at maximum energy. While a higher energy improves penetration and reduces scattering, the longer path length at this depth introduces image degradation. The absolute differences along the cube edges were more pronounced at 32 cm than at 16 cm. The cumulative scattering at greater depths caused more degradation around the periphery of the cube, although the differences remained smaller than those observed at lower energies, indicating improved boundary resolution.

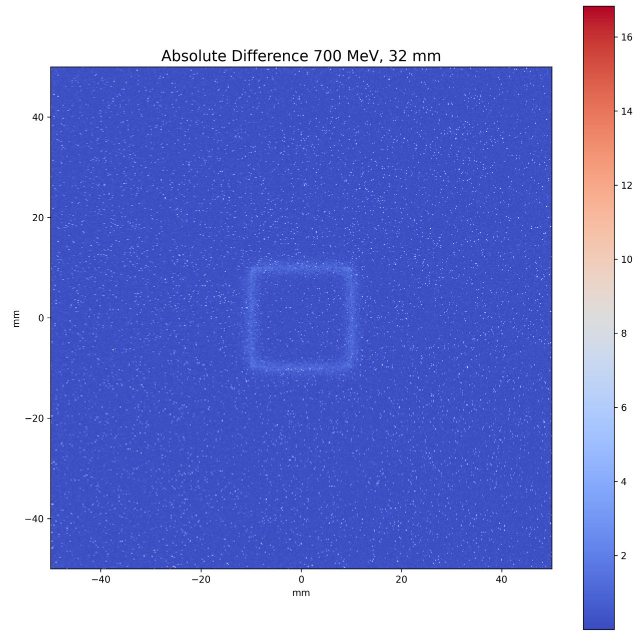

FIG. 16: Absolute Difference Image at 700 MeV, 32 cm thickness

In the central regions, the differences were reduced, but not as much as those at shallower depths. This suggests that even at 700 MeV, the longer path length introduces ambiguities, affecting the system's ability to reconstruct even details at the center. The histogram shows a wider spread of values compared to the 16 cm depth.

Overall, higher proton energies, particularly 700 MeV, enhance the spatial resolution by reducing scattering and improving object boundary accuracy, especially at shallower depths. However, at 32 cm, a longer path length leads to some degradation, particularly at the edges. The optimal energy range for thick object imaging appears to be between 600-700 MeV.

The analysis of intermediate energies (330, 400, 500, and 600 MeV) supports this trend. As the energy increased from 330 MeV to 600 MeV, the edge sharpness improved and scattering effects were reduced, particularly at a depth of 16 cm. The difference images at 500 and 600 MeV showed significantly smaller discrepancies, confirming the enhanced resolution. However, at a depth of 32 cm, blurring persisted at lower energies, such as 330 and 400 MeV, owing to cumulative scattering.

B. CNR and Dose Analysis

To evaluate the performance of the imaging system beyond spatial resolution, both Contrast-to-Noise Ratio (CNR) and dose deposition were analyzed at different proton beam energies and thicknesses. While the Modulation Transfer Function (MTF) provides insights into spatial detail preservation, the CNR assesses the system's ability to distinguish between materials, such as the aluminum cube and the surrounding medium. Dose calculations quantify the energy deposited in the phantom and provide a measure of radiation exposure due to imaging.

Simulations were conducted with different particle counts (5×10^5, 5×10^6, 10^6, and 10^7 protons) at all energy levels for a thickness of 16 cm, allowing for an evaluation of the impact of proton count on image contrast, noise, and dose deposition.

1. *Energy and Particle Count Correlations*

At 250 MeV, increasing the particle count from 5×10^5 to 10^7 significantly increased the CNR from 5.54 to 24.62. This improvement is attributed to the reduced statistical noise with higher particle counts, though it also results in increased dose deposition.

A similar trend was observed at 330 MeV, where the CNR at 10^7 particles reached 18.80, higher than at lower particle counts but still lower than the corresponding values at 250 MeV. This indicates that, while higher particle counts improve contrast, increasing the energy reduces the system's ability to fully distinguish contrast details.

As the energy increased to 400 MeV and above, this trend continued. At 700 MeV, the CNR peaks at 9.09 for the highest particle count, significantly lower than at 250 MeV, despite a much higher particle count. This suggests that although higher-energy protons reduce scattering and improve penetration, the system's contrast resolution diminishes owing to particle losses due to nuclear interactions.

2. *Dose-CNR Trade-off*

As the particle count increases, both the CNR and absorbed dose increase, creating a trade-off between the image quality and radiation exposure. As CNR is affected both by particle count (and imaging dose by extension) and imaging energy, these parameters need to be explored together to assess possible trade-offs.

At 250 MeV, the CNR peaks at 24.62 for 10^7 particles, but the dose reaches 7.58×10^{-3} Gy (7.58 cGy). In contrast, for 5×10^5 particles, the dose was much lower at 3.79×10^{-4} Gy (0.379 cGy), although the CNR dropped to 5.54. This demonstrates the trade-off: increasing the particle count improves contrast but also raises the dose, which can be of concern in clinical settings.

This trade-off becomes more pronounced as the energy level increases. At 330 MeV, raising the particle count from 5×10^5 to 10^7 improves CNR from 4.30 to 18.80, but the dose increases from 3.24×10^{-4} Gy to 6.48×10^{-3} Gy. A similar trend occurs at 400 MeV, where CNR rises from 3.65 to 15.92, and dose increases from 2.98×10^{-4} Gy to 5.96×10^{-3} Gy.

Interestingly, at 700 MeV, while the dose (5.19E-03 Gy) was lower than that at 250 MeV for the same particle count, the CNR reached only 9.09, indicating that a higher energy does not always result in proportional CNR improvements. This suggests that while higher energies provide deeper penetration, they do not necessarily enhance the contrast at higher doses, due to increased particle loss in inelastic nuclear interactions.

3. Optimal Energy for CNR and Dose Balance

Identifying the optimal energy that balances high contrast with low radiation exposure is important for both clinical and research applications. The graphical analysis in Figure 17 visually represents how energy levels affect the relationship between the CNR and the dose for various proton counts. At lower energies, such as 250 and 330 MeV, the CNR increases significantly with higher particle counts, but the dose rises steeply. For instance, at 250 MeV, the CNR peaks at 24.62 for a dose of 7.58 cGy, the highest value observed across all energy levels, but with a higher dose. At 330 MeV, the CNR reaches 18.79 at a lower dose of 6.48 cGy, offering a better balance between contrast and dose.

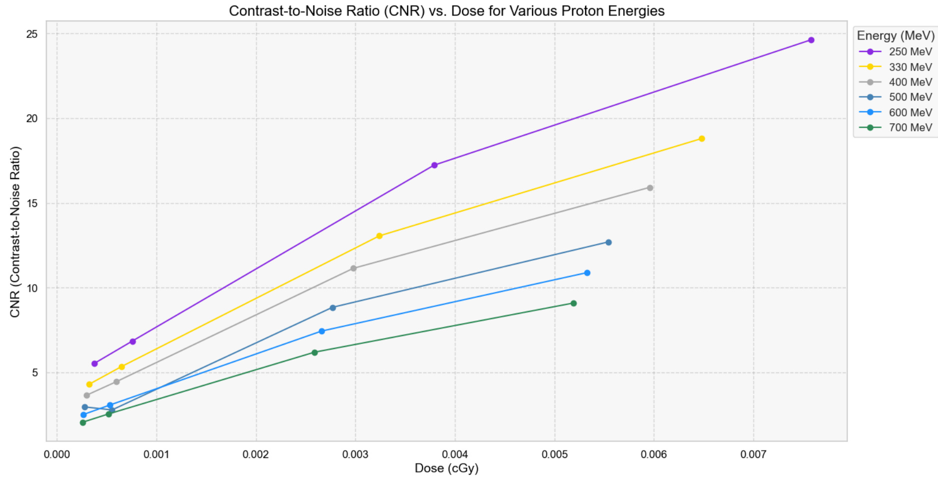

FIG. 17: Contrast-to-Noise Ratio (CNR) vs. Dose for Various Proton Energies.This figure shows the relationship between the Contrast-to-Noise Ratio (CNR) and dose across a range of proton energies. The graph highlights how the CNR changes with increasing dose for each energy level, providing insights into the trade-off between image quality and radiation exposure at different proton beam energies.

As the energy increased to 400 MeV and beyond, the improvement in the CNR slowed relative to the increase in dose. For example, at 400 MeV, the CNR is 15.92 for a dose of 5.96 cGy, providing a good contrast with the reduced dose at a dose. This trend continues at 500 MeV and 600 MeV, where further CNR improvement becomes marginal despite the increasing dose, suggesting that the CNR enhancement plateaus beyond 400 MeV.

At 700 MeV, CNR increases with particle count but remains lower than those at 250 and 330 MeV. For instance, the CNR reaches 9.09 at 5.19 cGy, reinforcing that while higher energies reduce proton drift and improve depth penetration, they may not maximize the contrast at shallower depths.

The graph highlights that 250 MeV and 330 MeV provide the highest CNR for the lowest dose in the low- to mid-dose range. However, for higher doses and larger particle counts, energies between 400 MeV and 600 MeV offer the best balance between contrast improvement and imaging dose.

C. Rejection Rate Analysis

1. *Rejection Rate by Energy and Phantom Thickness*

This aspect evaluates the rejection rate of particles to assess the effectiveness of energy filtering and count of particles relevant for reconstruction algorithm, which in turns impacts the necessary imaging dose . Table III presents the rejection rates for the filters of energy, particle counts, and relative angle for thickness of 16 cm across different energy levels from 250 to 700 MeV.

TABLE III: Filter rejection Rates for 16 cm Thickness for Different Proton Energies

Energy (MeV)	Energy Filter Rejection Rate (%)	Counts Filter Rejection Rate (%)	Relative Angle Rejection Rate (%)
250	12.58	12.58	18.93
330	14.97	14.97	20.94
400	16.75	16.75	23.02
500	19.28	19.28	25.46
600	22.68	22.68	28.82
700	25.03	25.03	31.44

As shown in Table III, the energy filter rejection rate increased consistently at higher energy levels. At 250 MeV, approximately 12.58% of the particles were rejected based on the energy criteria, which increased to 25.03% at 700 MeV. This trend reflects the increasing number of particles undergoing inelastic scattering interactions, which necessitate stricter filtering for imaging accuracy. As the last filter, relative angle filter mainly rejects large-angle MCS events. It can be seen that for 250 MeV, additional 6.35% of particles are rejected after first 2 filters, while for 700 MeV - 6.41%. Furthermore, there is no significant variation in this additional rejection based on relative angle with increasing proton energy. A similar trend was observed for a phantom thickness of 32 cm. The particle rejection rate increased from 9.46% at 250 MeV to 29.16% at 700 MeV Table IV, reflecting the increased particle loss due to inelastic nuclear interaction. Interestingly, for this phantom thickness there is variation in the additional rejection rate after relative angle filtering - 15% of events are additionally reduced after relative angle filter at 250 MeV, while for 700 MeV the rate has increased to 18.96%. This change, compared to 16 cm phantom thickness could be attributed to loss of efficiency of energy filtering at higher energies for thick geometries, which then must further corrected by the relative angle filter.

TABLE IV: Energy and Rejection Rates at 32 cm Depth for Different Proton Energies

Energy (MeV)	**Energy Filter Rejection Rate (%)**	**Counts Filter Rejection Rate (%)**	**Relative Angle Rejection Rate (%)**
250	9.46	9.54	24.46
330	12.83	12.83	30.22
400	13.21	13.21	34.65
500	16.10	16.10	39.37
600	22.85	22.85	44.26
700	29.16	29.16	48.12

Overall, the analysis showed a consistent increase in the rejection rates for energy and relative angle (for 32 cm thickness) filters with increasing proton imaging energy. This trend was more pronounced at a depth of 32 cm than at 16 cm, highlighting the challenges of particle loss for thicker geometries due inelastic nuclear interactions. It should be noted that increased rejection rates at higher energies indicate that more primary particles are necessary to maintain image quality - phenomenon which was shown already for CNR analysis. Higher imaging energies necessitate the increase of primary particles, thus - the imaging dose - in order to maintain parameters as CNR and WEPL uncertainty to a similar level of lower energies.

D. WEPL Accuracy Assessment

1. WEPL Accuracy and Uncertainty Analysis

For WEPL accuracy analysis, we assessed the percentage uncertainty in both the aluminum and water regions using simulations with 10^7 particles. The analysis aimed to quantify the uncertainty of the data-processing method for each region, considering the differences in proton interactions between high-density (aluminum) and low-density (water) materials.

As shown in Table V, percentage uncertainty consistently increased with energy in both regions. At lower energies, such as 250 MeV, the system maintained a relatively low uncertainty; however, at 700 MeV, the uncertainties became more pronounced.

The uncertainties in the aluminum region started at 2.24% at 250 MeV and increased to 4.77% at 700 MeV. In the water region, the uncertainties were similar to those in aluminum at

TABLE V: WEPL Uncertainty for Aluminium and Water Regions

Energy (MeV)	**Total Uncertainty (%)**	**Aluminum Region Uncertainty (%)**	**Water Region Uncertainty (%)**
250	2.24	2.24	2.09
330	2.84	2.84	2.75
400	3.36	3.36	3.29
500	4.09	3.67	4.04
600	4.81	4.25	4.79
700	5.53	4.78	5.54

250 MeV, starting at 2.09%, but increased more sharply to 5.54% at 700 MeV. This highlights the growing challenge of accurately resolving the WEPL at higher energy levels, due to increased particle loss due to rejection in filtering stage, as well as the WEPL sensitivity to small energy changes at higher imaging energies. Similarly as rejection rate analysis, this finding also clearly indicates that higher imagine energies would require increased imaging dose to increase counts in each of the pixels, thus limiting the uncertainty of PR images.

E. Low-Contrast Resolution Assessment

1. *Comparison of Low-Contrast Phantom Images*

After analyzing the spatial resolution, we evaluated the ability of the system to distinguish low-contrast materials by generating different images, while also employing pixel-wise filtering for energy values, compared to Gaussian fit method in simpler geometries.

At 250 MeV and 16 cm thickness, the absolute difference map in Figure 18 shows significant variations in the contrast resolution across different phantom materials. The largest WEPL deviations, up to 0.5 mm, were observed for the smallest cylinders (0.5 mm and 2 mm), representing the lung (ICRP -1%) and adipose tissue. These materials with lower RSP values are more susceptible to scattering, which is amplified at lower proton energies. This increased scattering reduces the ability of the system to resolve smaller structures.

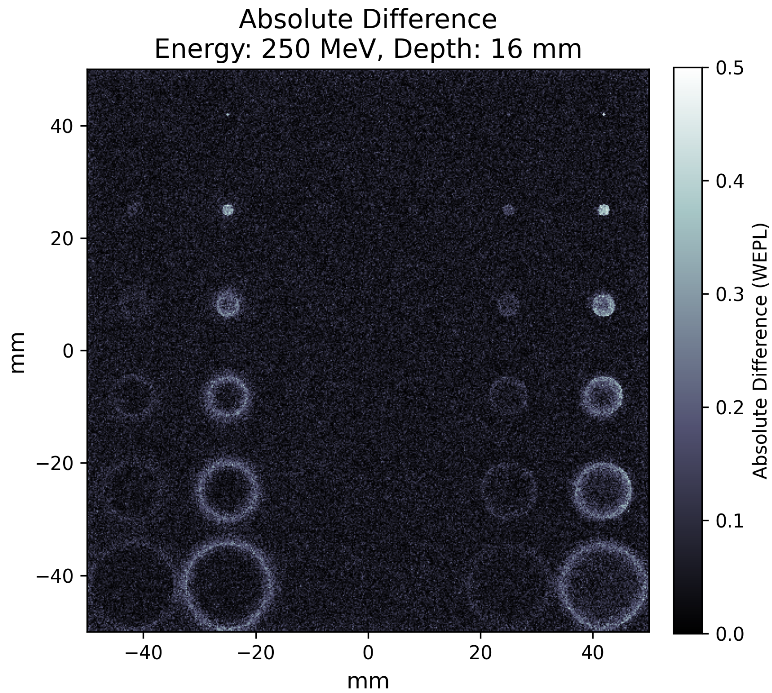

FIG. 18: Absolute WEPL Differences at 250 MeV and 16 cm thickness

In contrast, larger cylinders, such as those with diameters of 10 mm and 15 mm, representing the bone (ICRU +2.5%) and brain (ICRP +0.5%), showed smaller WEPL deviations. These high-RSP materials, along with their larger sizes, experience less scattering, thus presenting improved contrast resolution.

The absolute difference results reinforce this observation: most deviations for larger objects were below 0.1 mm, while deviations up to 0.5 mm were primarily associated with smaller, low-RSP cylinders, where scattering complicates contrast resolution. At 250 MeV and 32 cm thickness, the absolute difference map in Figure 19 reveals a similar pattern to the 16 cm thickness, but with more pronounced discrepancies in contrast resolution. The smallest cylinders, particularly those representing the lungs (ICRP -1%) and adipose tissue, again showed the largest WEPL deviations, up to 0.5 mm. For this thickness, the combination of lower energy and increased scattering further complicates the resolution of the smaller structures with low RSP values.

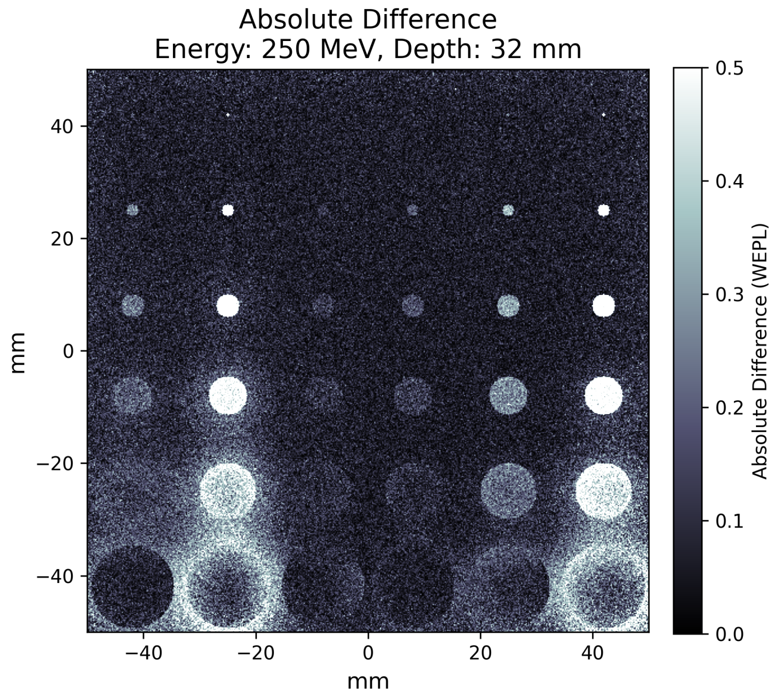

FIG. 19: Absolute WEPL Differences at 250 MeV and 32 cm thickness

For larger cylinders, such as those representing the bone (ICRU +2.5%) and brain (ICRP +0.5%) with diameters of 10 mm and 15 mm, the contrast resolution improved. However, slightly higher WEPL deviations were noted at 32 cm than at 16 cm, reaching up to 0.3 mm. This indicates that as the depth increases, scattering accumulates and affects the system's ability to maintain consistent reconstruction of WEPL, thus - contrast resolution, even for higher RSP materials.

The absolute difference map shows a wider distribution of deviations at this phantom thickness, with most values clustering between 0.1 mm and 0.3 mm. A small number of deviations exceed 0.5 mm, reflecting the more challenging low-RSP materials with smaller diameters.

At 700 MeV and 16 cm thickness, the absolute difference map in Figure 20 shows significantly smaller WEPL deviations than those at 250 MeV. The higher proton energy reduces scattering, thus resulting in more accurate contrast resolution across different materials, as individual objects are less influenced by surrounding media. For the smallest cylinders, representing the lung (ICRP -1%) and adipose tissue, WEPL differences rarely exceed 0.1 mm.

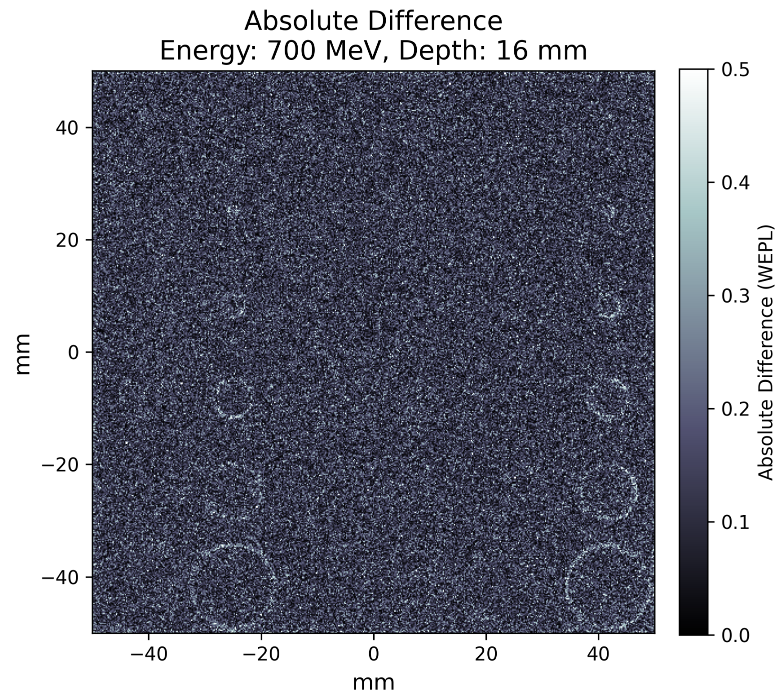

FIG. 20: Absolute WEPL Differences at 700 MeV and 16 cm thickness

For larger cylinders, such as those representing the bone (ICRU +2.5%) and brain (ICRP +0.5%) with diameters of 10 mm and 15 mm, the WEPL differences were minimal, staying below 0.05 mm. The ability of the system to maintain contrast resolution for these higher RSP materials was significantly improved at this energy level.

The absolute difference map shows that most deviations are clustered below 0.1 mm, with only a few outliers. The shorter tail of the histogram compared with the lower-energy cases confirms the consistent performance at higher energies.

At 700 MeV and 32 cm thickness Figure 21, similar trends were observed at 16 cm, although with slightly larger discrepancies owing to the increased thickness. A higher proton energy effectively maintains the contrast resolution across different materials, even with increased scattering. For the smallest cylinders, representing lung (ICRP -1%) and adipose tissue, WEPL differences remained small, not exceeding 0.3 mm, showing that high energy mitigates cumulative cattering effects that would cause larger deviations at lower energies.

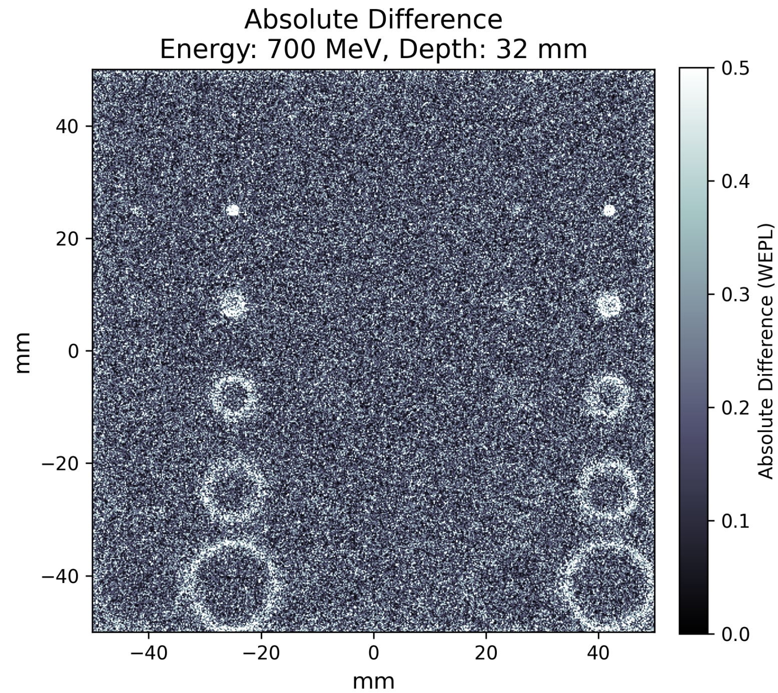

FIG. 21: Absolute WEPL Differences at 700 MeV and 32 cm thickness

For larger cylinders, such as those representing bone (ICRU +2.5%) and brain (ICRP +0.5%) with diameters of 10 mm and 15 mm, WEPL differences remained minimal, generally below 0.1 mm, demonstrating the system's effectiveness at this energy level, even at greater depths.

In the intermediate-energy range (330–600 MeV), the contrast resolution gradually improved as the proton energy increased. At 330 MeV, lower-RSP materials, such as lung and adipose tissue, still showed notable WEPL deviations, especially at a depth of 32 cm, although the performance was better than at 250 MeV. Scattering was still significant, particularly for the smaller cylinders. As the energy increased to 400 MeV, deviations across all materials, including the bone and brain, were reduced, and scattering became less prominent at both depths.

At 500 MeV, minimal WEPL deviations were acchieved across all materials and cylinder sizes, even for smaller structures within thicker geometries. By 600 MeV, the contrast resolution improved further with consistently low WEPL differences, even for the smallest cylinders at a depth of 32 cm. This energy level shows the system's strong ability to resolve fine contrasts while effectively mitigating scattering effects.

What should be noted for this analysis though, the analysis here assumes infinitely small, idealized energy resolution of the detector. This aspect is given in more detail in later sections of the work. As there is limited energy resolution of the detecting system, the improved performance seen for higher energies would actually be lost in a realistic scenario and contrast resolution would actually be reduced for higher energies. As the stopping power of protons remains rather constant at high imaging energies, small energy exiting particle energy deviations actually reflect large variations in WEPL. Thus, highly sensitive energy detectors would be necessary for high energy proton radiography, which could not be feasible with the the current technological capabilities.

2. Qualitative Contrast Resolution Analysis

This section evaluates qualitatively the impact of proton energies (250–700 MeV) and phantom thicknesses (16 and 32 cm) on material visibility within the cylindrical phantom.

At 250 MeV, significant scattering was observed, especially with smaller low-RSP cylinders, such as the lung (-1%) and adipose tissue (-0.5%). For a thickness of 16 cm, these materials appeared blurred, and the 0.5 mm and 2 mm cylinders were difficult to resolve. Cylinders of higher diameter had better visibility, although the contrast was still limited by scattering.

For a thickness of 32 cm, with scattering intensified, smaller cylinders were not indistinguishable and reducing visibility for larger diameters, as well. This highlights the limitations of 250 MeV in resolving the contrast and detail for objects of larget thickness.

At 330 MeV, the resolution improved slightly, with clearer visibility for the 2 mm and 4 mm cylinders for 16 cm, although smaller structures still pose challenges. Larger high-RSP cylinders, such as bone and brain, were more distinguishable, with sharper boundaries. For 32 cm thickness, smaller cylinders remained unresolvable.

At 400 MeV, the contrast resolution noticeably improved, particularly for 16 cm. Smaller cylinders, such as the 2 mm adipose (-0.5%) and 4 mm muscle (+1%) cylinders, were more distinguishable with less blurring. With reduced scattering, better visibility of medium and larger cylinder diameters was achieved. For 32 cm, medium and larger diameter cylinders remained visible, although smaller cylinders were still not fully resolvable.

At 500 MeV, the resolution improved across all cylinder sizes. The smallest cylinders (0.5 mm and 2 mm) had clearer boundaries and decreased noise. Larger diameter cylinders retained excellent contrast and minimal blurring. Even at 32 cm, medium-sized cylinders (4 and 7 mm) remained clearly visible, with larger cylinders maintaining sharp boundaries. With decreased scattering at this energy level, better contrast resolution is achieved.

At 600 MeV, the contrast resolution improved further, particularly for 16 cm. The smallest cylinders (0.5 mm and 2 mm), were much clearer to distinguish with minimal blurring. Medium and larger cylinders (4, 7, 10, and 15 mm) were well resolved with almost no blurring.

For 32 cm, the system continued to perform well, with only slight blurring in the smaller cylinders owing to increased scattering due to traversal of thicker medium. Medium and larger cylinders retained sharp boundaries and good contrast, with 600 MeV offering better resolution than observed at lower energies.

At 700 MeV, the system reached its peak performance in terms of low contrast detail resolution. Even the smallest cylinders were clearly visible for 16 cm, with minimal noise and strong contrast for the medium and larger cylinders. Scattering was minimal, delivering the best overall low contrast resolution across all materials. For 32 cm, while smaller cylinders showed some blurring, medium and larger cylinders remained clearly visible, confirming that higher energies such as 700 MeV are effective for resolving fine details at greater depths.

In summary, 600 MeV and 700 MeV provided the best performance in terms of low contrast resolution, especially for a thickness of 16 cm. For 32 cm, smaller structures remained challenging to resolve, however, at these higher energies good contrast and visibility sustained , with 700 MeV delivering the best performance.

3. WEPL Accuracy Based on Energy and Phantom Thickness

This subsection evaluates how different proton energies (250–700 MeV) and phantom thickness (16 cm and 32 cm) affect WEPL accuracy within images acquired with low contrast resolution images.

[11]Six NIST materials that represented various contrasts within low contrast resolution phantom were analyzed in terms of WEPL accuracy achieved in radiographic images.

At 250 MeV, scattering significantly affected resolution of lighter materials, such as lung and adipose tissue, leading to slight deviations from theoretical WEPL values, as indicated in Table VI. For lung tissue at 16 cm thick phantom with a 0.7 cm cylinder, the measured WEPL was 16.057 ± 0.054, compared to the expected value of 15.84, indicating the impact of scattering on accurate estimation of WEPL values. Adipose tissue with a 1 cm cylinder showed a measured WEPL of 16.175 ± 0.079 (expected 15.92). For 32 cm thickness, when scattering becomes more pronounced, with lung tissue measuring 32.167 ± 0.139 (expected 31.68), and adipose tissue at 32.441 ± 0.17 (expected 31.84).

TABLE VI: WEPL Accuracy for 250 MeV and 330 MeV Proton Energies in Lung and Adipose Tissues for Different Phantom Thicknesses

Energy (MeV)	**Material**	**Cylinder Diameter (cm)**	**Phantom thickness (cm)**	**Expected WEPL**	**Measured WEPL (cm)**
250	Lung (-1%)	0.7	16	15.84	16.057 ± 0.054
250	Adipose Tissue (-0.5%)	1	16	15.92	16.175 ± 0.079
250	Lung (-1%)	0.7	32	31.68	32.167 ± 0.139
250	Adipose Tissue (-0.5%)	1	32	31.84	32.441 ± 0.17
330	Lung (-2.5%)	0.7	16	15.6	16.027 ± 0.116
330	Adipose Tissue (-0.5%)	1	16	15.92	16.188 ± 0.103
330	Lung (-2.5%)	0.7	32	31.2	32.188 ± 0.219
330	Adipose Tissue (-0.5%)	1	32	31.84	32.527 ± 0.138

At 330 MeV, the scattering is reduced, but it still affects lighter materials. Lung tissue for 16 cm thickness (0.7 cm cylinder) showed a measured WEPL of 16.027 ± 0.116 (expected 15.6), and adipose tissue (1 cm cylinder) measured 16.188 ± 0.103 (expected 15.92). For 32 cm thickness, lung tissue measured 32.188 ± 0.219 and adipose tissue 32.527 ± 0.138, both slightly exceeding the expected values.

At 400 MeV, the scattering is significantly reduced compared to that at 250 and 330 MeV. For the brain tissue (1 cm cylinder) at a depth of 16 cm, the measured WEPL was 16.001 ± 0.148, close to the expected value of 16.08, indicating that higher energy reduces WEPL value deviations from expected values. Similarly, muscle tissue (1.5 cm cylinder) showed a measured WEPL of 16.003 ± 0.139 (expected 16.16), confirming that WEPL accuracy is increased at higher energies due to decreased scattering. Table VII.

For 32 cm thickness, in the brain tissue (1 cm cylinder), with a measured WEPL of 30.35 ± 7.593, significantly below the expected 32.16, and a large standard deviation highlighting cumulative scattering. Muscle tissue (1.5 cm cylinder) showed a measured WEPL of 31.611 ± 4.436 (expected 32.32).

TABLE VII: WEPL Accuracy for 400 MeV and 500 MeV Proton Energies in Brain and Muscle Tissues for Different Phantom Thicknesses

Energy (MeV)	**Material**	**Cylinder Diameter (cm)**	**Phantom thickness (cm)**	**Expected WEPL**	**Measured WEPL (cm)**
400	Brain (+0.5%)	1	16	16.08	16.001 ± 0.148
400	Muscle (+1%)	1.5	16	16.16	16.003 ± 0.139
400	Brain (+0.5%)	1	32	32.16	30.35 ± 7.593
400	Muscle (+1%)	1.5	32	32.32	31.611 ± 4.436
500	Brain (+0.5%)	1	16	16.08	15.991 ± 0.188
500	Muscle (+1%)	1.5	16	16.16	16.005 ± 0.184
500	Brain (+0.5%)	1	32	32.16	32.038 ± 0.331
500	Muscle (+1%)	1.5	32	32.32	32.063 ± 0.364

At 500 MeV, the WEPL accuracy improved further, particularly at lower thicknesses. Brain tissue (1 cm cylinder) for 16 cm thickness showed a WEPL of 15.991 ± 0.188, closely matching the expected value of 16.08, and muscle tissue (1.5 cm cylinder) measured 16.005 ± 0.184 (expected 16.16). For 32 cm thickness, both the brain and muscle tissues showed values closer to the expected values than at 400 MeV. Brain tissue (1 cm cylinder) had a WEPL of 32.038 ± 0.331 (expected 32.16), and muscle tissue (1.5 cm cylinder) measured 32.063 ± 0.364 (expected 32.32). This demonstrates that 500 MeV provides better WEPL accuracy at greater thicknesses, thereby minimizing the scattering observed at lower energies.

At 600 MeV and 700 MeV, the scattering effects are further minimized, improving the WEPL accuracy, particularly in denser materials such as bone Table VIII. Therefore, these energy levels are well suited for improved WEPL accuracy in denser tissues, with smaller deviations observed between the measured and expected WEPL values, even at greater thicknesses.

At 600 MeV, the WEPL accuracy was excellent for both 16 cm and 32 cm thicknesses. For a 1 cm bone cylinder at a phantom of thickness 16 cm, the measured WEPL was 15.973 ± 0.222 (expected 16.4), and for the 1.5 cm cylinder, it was 16.022 ± 0.191 (expected 16.4). At 32 cm thickness, deviations increased slightly, with the cylinder measuring 32.086 ± 0.334 (expected 32.8) and the 1.5 cm cylinder measuring 32.019 ± 0.369, still within an acceptable range considering the phantom thickness.

At 700 MeV, a similarly high accuracy was observed. For the 1 cm bone cylinder at phantom of thickness 16 cm, the WEPL was 15.945 ± 0.214 (expected 16.4), and for the 1.5 cm cylinder, 15.972 ± 0.219 (expected 16.4). At 32 cm thickness, the WEPL accuracy

TABLE VIII: WEPL Accuracy for 600 MeV and 700 MeV Proton Energies in Bone Tissue for Different Phantom Thicknesses

Energy (MeV)	Material	Cylinder Diameter (cm)	Phantom thickness (cm)	Expected WEPL	Measured WEPL (cm)
600	Bone (+2.5%)	1	16	16.4	15.973 ± 0.222
600	Bone (+2.5%)	1.5	16	16.4	16.022 ± 0.191
600	Bone (+2.5%)	1	32	32.8	32.086 ± 0.334
600	Bone (+2.5%)	1.5	32	32.8	32.019 ± 0.369
700	Bone (+2.5%)	1	16	16.4	15.945 ± 0.214
700	Bone (+2.5%)	1.5	16	16.4	15.972 ± 0.219
700	Bone (+2.5%)	1	32	32.8	31.878 ± 0.388
700	Bone (+2.5%)	1.5	32	32.8	31.952 ± 0.377

remained high, even though the increased cumulative effect of scattering. The 1 cm cylinder measures 31.878 ± 0.388 (expected 32.8), and the 1.5 cm cylinder records 31.952 ± 0.377, slightly below the expected value. Despite these minor deviations, 700 MeV provides excellent resolution for imaging of larger objects, maintaining high accuracy even for thicker phantom sizes.

F. WEPL resolution analysis: energy resolution and depth resolution limited

This section evaluates the system's ability to resolve subtle changes in WEPL by examining two key aspects: the influence of a 1% energy resolution on the depth resolution, and the capacity of the system to distinguish tissue WEPL variation for different phantom thicknesses. The goal was to determine the depth resolution necessary to detect a 2 mm change in WEPL, selected as an optimal benchmark within a relevant range of 1-3 mm. This reflects the challenges in detecting small WEPL variations, which is an essential requirement for accurate images for patient positioning.

The central energy values, along with their lower and upper bounds, were used to calculate the WEPL resolution across the energy limit of +/- 1%. For thickness of 160 mm, the resolvable WEPL difference increased to 3.81 mm at 250 MeV compared to 1.09 mm at 320 mm thickness, as shown in 22a. This illustrates the inverse relationship between phantom thickness and achievable WEPL resolution, which worsens for smaller size phantoms. At higher energies such as 700 MeV, the WEPL resolution was significantly worse, as indicated in 22b. For example, at 700 MeV, the WEPL resolution achievable with 1%

energy resolution is approximately 24.68 mm for phantom thickness of 320 mm. This is unacceptable WEPL resolution as it is far beyond the necessities of clinical imaging system. These results suggest that either lower imaging energy should be used or high resolution energy detectors are necessary. Following this analysis, the inverse problem was assessed. The energy resolution required from a detector to detect a 2 mm change in WEPL was analysed. This threshold was selected to evaluate the system sensitivity to small variations that are of clinical relevance. At 250 MeV, the energy resolution required to detect the 2 mm change was the highest. For a phantom of thickness of 320 mm, the required resolution was 1.83% compared to 0.52% at a depth of 160 mm.

As the energy increased to 330 MeV, the required energy resolution decreased to 0.41% at a depth of 320 mm and to 0.27% at a depth of 160 mm. This trend continued with an increase in the energy. At 500 MeV, the resolution required for a 2 mm change dropped to 0.15% at a depth of 320 mm and 0.12% at a depth of 160 mm. At 700 MeV, the energy resolution required was minimal at 0.08% for a depth of 320 mm and 0.07% for a depth of 160 mm. Energy resolution analysis showed that at lower energies, detectors with relatively low (¿ 1%) energy resolution can be used for particle radiography. Going towards higher imaging energies clearly show the need for increased resolution of the energy detectors in order to detect clinically relevant WEPL changes (of 2 mm). It must be noted that, the energy resolution requirements for highest energies cannot be easily met with current detector technological capabilities. Although the approach of direct range detectors could be taken, they would suffer of range straggling at higher energies, which again translate into increased uncertainty of WEPL. Therefore, this analysis clearly shows that although higher energy protons offer greatly increased spatial resolution, clinical applicability would be limited by WEPL resolution achievable. This indicated that an optimum energy would be lower than 700 MeV, possibly looking in the range of 330-250 MeV.

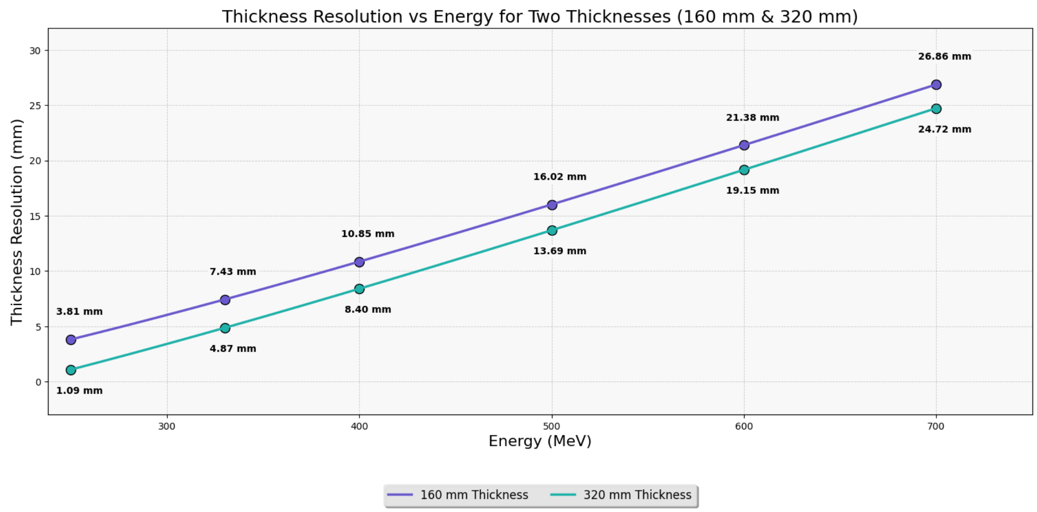

(a) Energy Resolution vs Energy

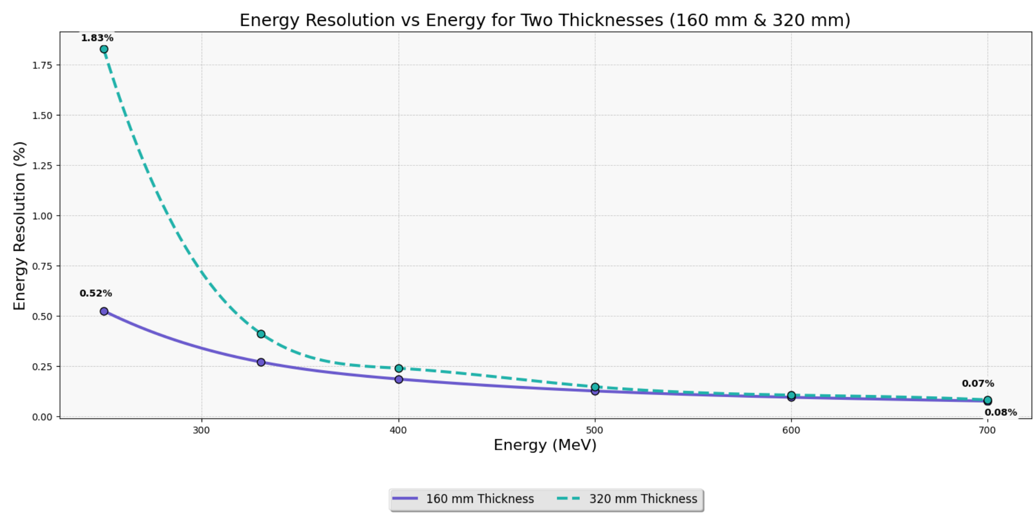

(b) Thickness Resolution vs Energy

FIG. 22: Comparison of Energy and Thickness Resolution for Different Phantom Thicknesses

G. RSP Analysis

[39]Although in typical clinical treatment planning process, RSP values are typically derived from X-ray CT, the differing interaction mechanisms between protons and X-rays can introduce uncertainties of up to 5% in the RSP estimations.

In this analysis, the RSP values were calculated for several biological tissues, including water, brain, bone, muscle, blood, lung, adipose tissue, and skin. These calculations, based on the [25]Bethe-Bloch equation, span a proton energy range of 50–700 MeV at 10 MeV intervals. The goal was to examine how RSP values calculated for proton beams of different energies - data that would be acquired with radiographical imaging - compare to the RSP calculated with the treatment beam of helium-4 ions. The RSP data were acquired by calculating the stopping power of each tissue and then normalizing it the value of water at each energy. RSP values were then normalized to helium at 100 MeV/u to compare RSP accuracy with increasing proton energy. Using helium stopping power as a reference, we evaluated whether RSP data acquired with proton beams (radiographic imaging) would be significantly different from RSP values of helium-4 ion beams (treatment beam).

Figure 23 illustrates several key trends on this matter. Cortical bone displayed the highest RSP values, which increased with proton kinetic energy. This was expected because of the bone's higher density and lower electron density, resulting in greater energy loss by protons.

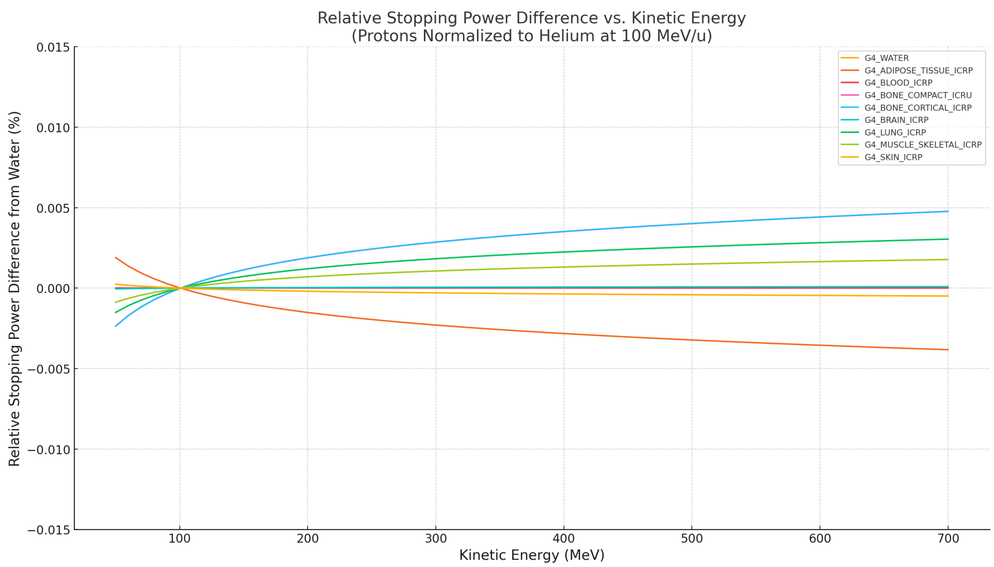

FIG. 23: Relative Stopping Power Difference Across Tissues vs. Kinetic Energy (Protons Normalized to Helium at 100 MeV/u). This figure presents the relative stopping power (RSP) differences for various tissues across a range of proton kinetic energies, normalized to helium at 100 MeV/u. The percentage difference relative to normalization RSP value of 100 MeV/u helium-4 ions is depicted, illustrating how different tissues interact with protons at varying energy levels, with denser tissues such as bone showing greater variation than softer tissues such as muscle and lung.

Soft tissues, such as blood, brain, and muscle, show minimal differences from normalization RSP value at different energy levels, reflecting their similar physical densities.

As proton energy increases, the differences compared to normalization RSP value become more pronounced, especially in denser tissues, such as bone. Below 100 MeV, most tissues exhibited minimal variation from normalization. However, at higher energies, the disparity grows, particularly in the bone.

The analysis suggests that, using higher proton energies in radiography slightly increases RSP value deviation from reference value at treatment beam energy. Despite that, the deviation is rather small, typically below 0.1 %, therefore it would not dramatically increase the uncertainty in particle therapy treatment. These small deviations still suggest the possible use of higher proton imaging energies due to favourable results of other image quality metrics.

VI. TECHNOLOGICAL CONSIDERATIONS IN PROTON IMAGING

A. Detector Technology Comparison

Although simulations form the basis of this study and provide a theoretical framework, their clinical application relies on appropriate detector technologies. These detectors play a key role in measuring the particle position, angle and energy for accurate imaging.

This section reviews detector technologies, including single particle tracking and integrating detectors, that provide information on particle position, angle and energy.

[40]In PR and proton computed tomography (PCT), various detector systems are used, each of which is suited to specific applications. Table IX summarizes the features of these technologies and highlights their benefits and limitations.

[40]Silicon strip detectors offer a high SNR and nearly 100% detection efficiency, making them highly precise for single particle tracking in PR. However, their small active area (typically 10×10 cm^2) and longer integration times can be limiting in applications that require faster data acquisition. Despite these challenges, precision remains a key benefit.

[40]Scintillating optical fibers paired with photomultiplier tubes (PMTs) or silicon photomultipliers (SiPMs) provide high spatial resolution and rapid data acquisition, thereby addressing the need for faster response times. These fibers are particularly useful in PR systems for efficient proton trajectory measurements. For example, the proton-VDA instru-

TABLE IX: Summary of Proton Radiography (PR) and Proton CT (PCT) Systems

Collaboration	**Type**	**Tracking Technology**	**Energy Detector Technology**	**Readout Rate**
[41]AQUA	PR	GEM	Scintillating Range Counter	10 kHz
[41]PSI	PR	Scintillating Fiber (Sci-Fi)	Scintillating Range Counter	1 MHz
[42]QBeRT	PR	Scintillating Fiber (Sci-Fi)	Scintillating Fiber Range Counter	1 MHz
[43]KVI-CART (University of Groningen)	PR	TPC based on GridPix	Crystal-Based Residual Energy Detector	100 Hz to 1 MHz
[41]LLU (Loma Linda University)	PR/PCT	Silicon Microstrip Detectors (SSD)	5-Stage Scintillator-Based WEPL Detector	>1 MHz
[44]OFFSET	PR	Scintillating Fiber (Sci-Fi)	None	1 MHz
[45]Bergen Collaboration	PR/PCT	Monolithic Active Pixel Sensors (MAPS)	High Granularity Tracking Calorimeter	2 kHz

ment uses scintillating fibers to reduce electronic complexity while maintaining throughput and accuracy.

[46] Monolithic active pixel sensors (MAPS) are a powerful solution to handle higher particle fluxes. Used in large-scale experiments such as CERN's ALICE detector, MAPS features fine segmentation with pixel sizes as small as $30 \times 27\ \mu\text{m}^2$. These sensors can manage high particle flux without degradation, although linking detection with tracking data remains a challenge for improving MLP estimations.

For large-area tracking, [41]micropattern gas detectors (MPGDs), including Gas Electron Multipliers (GEM) and micromegas, provide effective coverage. These detectors use gas amplification for fast signal generation and are ideal for high-resolution imaging tasks, such as proton CT. Their large coverage and fine segmentation make them suitable for large-scale proton imaging.

1. *Single Particle Tracking vs Integrative Detection Systems*

In PR, tracking detectors monitor particle trajectories as they pass through object. Tracking detectors register the position and angle at the entrance and exit of path through object, which is an information used for image reconstruction. Tracking detector always accompanied by an energy or range detector to measure residual energy, except in integrating PR approaches.

Although this review focuses on PR, heavier ions, such as carbon and helium, offer alternative approaches. [40]Carbon ions scatter less than protons but experience nuclear fragmentation, which requires specialized detector setups. Helium ions, with reduced nuclear fragmentation and scattering, behave similarly to protons, while providing increased spatial resolution, making them a viable option for clinical use.

PR detectors and general approaches fall into two categories: integrating and single particle tracking systems.

[47]Single particle tracking systems record the trajectory and energy of each proton, with the remaining energy measured by a calorimeter or range detector. The water-equivalent thickness (WET) is then calculated based on the registered energy. This method offers high spatial resolution but increases the imaging time, system complexity, and costs owing to the advanced electronics required.

[47]Integrating detection systems measure the flux of protons in a broad area or specific spots using devices such as ionization chambers, 3D scintillators or amorphous silicon panels to calculate the WET from dose profiles, 3D dose distributions or time-varying dose intensity profiles, if a special modulator wheel is used. Although faster and more cost-effective, these systems compromise spatial resolution and may require higher proton doses for adequate image quality.

2. *Energy and Range Detection in PR Systems*

Calorimeters measure the energy of outgoing protons by stopping them and producing a signal proportional to their energy, providing an assessment of the residual energy after the proton exits the patient. However, in thin phantoms with high residual energy, calorimeters face challenges due to energy resolution limitations, leading to increased uncertainty in low-WEPL measurements.

In contrast, range detectors only measure the proton-stopping depth. The WEPL precision in range detectors is affected by range straggling, which introduces statistical fluctuations in the stopping depth. [5]Additionally, the thickness of the telescope layers can affect the accuracy, with thicker layers (over 3 mm) introducing uncertainties.

WEPL resolution and accuracy is also highly dependent on the imaging energy, as higher energy resolution is necessary for the detector at higher energies. This is due to decreased stopping power at high proton energies, therefore smaller variations in exiting particle kinetic energy corresponds to large variations in measured WEPL values.

Two additional factors influence WEPL accuracy: the uncertainty in the initial proton energy and the number of protons used. Although increasing the number of protons improves precision (with the standard error decreasing as $\sqrt{n}$), it also increases the patient's dose and acquisition time.

3. *Operational Requirements for PR Systems*

The development of a clinically viable PR scanner requires addressing several technical and operational challenges. The primary focus is to achieve high-speed data acquisition to ensure that scans are completed in less than a minute. Efficient management of [41]proton fluxes between 5×10^6 to 15×10^6 particles per second, depending on the aperture size, requires a robust data acquisition system capable of processing large data volumes in real time.

Reducing the scan time to less than 5–10 min may require faster detectors or alternative WEPL detectors that are capable of measuring multiple protons simultaneously. Providing adequate beam energy allows protons to traverse the phantom in a single direction, which is necessary for maintaining imaging efficiency and precision. Close integration with beam-delivery systems synchronizes data acquisition with the timing and intensity of the proton beam, enabling accurate tracking of proton trajectories and precise energy deposition measurements to preserve image quality.

Managing clinical-level pencil beams also requires detector systems that can simultaneously track multiple protons to ensure precise image reconstruction. Achieving RSP accuracy better than 1% and spatial resolution around 0.5 mm reduces imaging artifacts and improves differentiation between tissue densities.

From a financial perspective, the development of a PR scanner involves substantial costs. To encourage widespread clinical adoption, the systems should remain affordable, [41]ideally between $100,000 and $200,000. This cost depends on factors such as the price of specialized components (e.g., silicon strip sensors and MAPS readout systems) and the degree of automation in production. Striking a balance between performance and affordability is the key to making PR scanners feasible for routine clinical use.

B. PR requirements in Synchrotron Design and Beam Parameters

Proton beam generation begins with a stable particle source, which is then accelerated to the required therapeutic energy. Although protons are widely used in PT, there is growing interest in heavier ions such as helium because of their reduced scattering and improved dose distributions.

After generation, protons must be accelerated to sufficient energy to effectively deliver the dose to the deepest part of the target area. The two main accelerator technologies used are cyclotrons and synchrotrons. Cyclotrons produce quasi-continuous high-current proton beams using a stationary magnetic field to guide particles in a spiral path. However, they generate fixed-energy beams, which require further modulation during treatment.

In contrast, [48] synchrotrons provide greater flexibility. Both the magnetic field and electric field oscillation frequencies were adjusted during acceleration, allowing for variable energy beams. This enables precise control over the depth and shape of the treatment area and improves the accuracy of the target. Once accelerated, a proton beam is delivered through a gantry or beamline system. Advanced scanning and beam modulation techniques ensure that the optimal dose is confined to the treatment area while minimizing exposure to surrounding healthy tissues.

1. Short overview of HeLICS Synchrotron Technology

The simulations conducted in this study tested proton energies potentially accelerated by the helium synchrotron developed by the Next Ion Medical Machine Study (NIMMS) group at CERN - HeLICS. This section evaluates the performance of this [7]compact synchrotron and its potential applications in PT. Designed for high efficiency, the synchrotron was optimized for accelerating both protons and helium ions, featuring a novel magnet design and an innovative injector linac. The technical specifications of the synchrotron are summarized in Table X.

TABLE X: Technical Specifications of the Compact Helium Synchrotron for Proton and Helium Therapy

Parameter	**Value**
Maximum Magnetic Rigidity	4.5 T/m
Maximum Energy (Helium Ions)	220 MeV/u
Maximum Penetration Depth	30 cm (in water)
Synchrotron Circumference	33 m
Magnet Maximum Field Strength	1.65 T
Average Power Consumption	170 kW
RF Frequency	352 MHz
Injection Energy (Helium Ions)	5 MeV/u
Extraction Method	Slow and Fast Extraction
Helium Ion Source Current	2 mA
Beam Intensity	8×10^{10} ions per cycle
Operational Duty Cycle	45% (protons), 50% (helium)
Applications	Proton/Helium Therapy, Research
Cooling Requirements	100 kW

The synchrotron offers both slow and fast beam extraction, providing flexibility for traditional radiotherapy, as well as more advanced techniques such as FLASH therapy. In addition, it supports mini-beam production and multi-ion operation, making it versatile for both imaging and treatment.

2. Required Beam Current and RF Frequency Calculations

An effective PT is based on synchronized acceleration within the synchrotron to ensure efficient beam delivery. The relationship between the proton energy and RF frequency requires precise adjustments to the electric field at higher energy levels to maintain synchronization with the accelerating magnetic field. For the higher proton energies investigated in the study, it might be necessary to increase the accelerating RF field frequency, compared to nominal one use for treatment mode.

Figure 24 illustrates this relationship, showing how the RF frequency increases proportionally with the proton energy. At lower energies, such as 250 and 330 MeV/u, the RF frequency begins at 3.170 MHz and gradually increases to 3.589 MHz, reflecting the moderate velocities of the protons. As the energy increases to 400 MeV/u and 500 MeV/u, the RF frequency jumps to 3.901 MHz and 4.286 MHz, indicating the growing need for higher RF frequency.

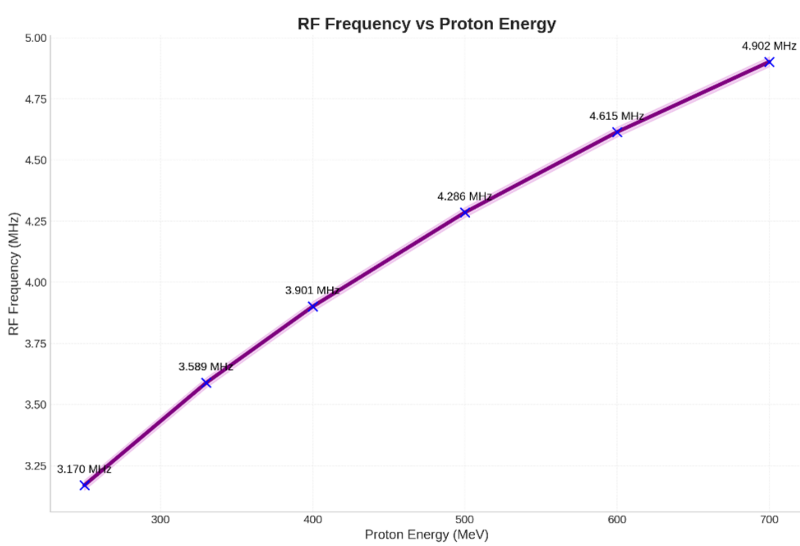

FIG. 24: RF Frequency Dependency on Proton Kinetic Energy in Compact Synchrotron Operation.This figure illustrates how the radiofrequency (RF) frequency changes as a function of the proton kinetic energy in a compact synchrotron. The graph demonstrates the proportional relationship between the increasing proton energy levels and the corresponding RF frequency adjustments required for precise beam synchronization during acceleration.

At higher energy levels, such as 600 and 700 MeV/u, the RF frequencies reached 4.615

MHz and 4.902 MHz, respectively. It clearly indicates the possible requirements for higher energy proton radiography to be implemented on helium synchrotron design, as current maximum RF frequency needed for treatment is lower.

Additionally, based on a detector read-out rate of 1 MHz Table IX, the beam current was calculated to be approximately 160 pA, corresponding to a particle count of 1 million particles per second.

VII. DISCUSSION AND CONCLUSIONS

Our simulations demonstrated that although higher-energy protons, particularly in the 600–700 MeV range, offer clear advantages in terms of depth penetration and scattering control, there are significant trade-offs when it comes to WEPL accuracy and energy resolution. Initially, we observed excellent spatial resolution and improved depth penetration at these energies; however, this was under idealized conditions, assuming an infinitely small energy resolution, something that is not feasible with current clinical detectors.

In practical terms, achieving reliable WEPL estimation at higher proton energies would require a remarkably high-energy resolution that exceeds the capabilities of existing clinical systems. Consequently, while higher energies improve spatial resolution, they also introduce significant inaccuracies in WEPL owing to detector limitations. This trade-off between better spatial resolution and poorer WEPL accuracy becomes critical as proton energy increases.

Thus, the optimal energy range for clinical proton radiography (PR) appears to be between 330 MeV and 500 MeV. Our simulations showed that, at these energies, a better balance is achieved between spatial resolution and WEPL accuracy, making them more practical for clinical applications. Although 600 MeV offers a good balance between reducing scatter and maintaining spatial resolution, particularly for dense tissues such as bone, WEPL degradation at these higher energies limits its reliability for accurate imaging at greater depths.

Another essential factor is the radiation dose. Our analysis indicated that higher-energy protons reduce the overall dose, but make it challenging to maintain high image quality, especially in terms of CNR. For example, at 250 MeV, we achieved a CNR of 24.62 with 10^7 particles, but this resulted in a dose of 7.58 cGy. In contrast, at 700 MeV, the dose dropped to 5.19 cGy, but the CNR decreased significantly to 9.09, highlighting the trade-off between dose and image quality. This suggests that mid-range energies (330-500 MeV) offer the most effective balance between contrast resolution and dose, making them more suitable for clinical use.

To ensure successful clinical integration of PR, several key areas must be addressed, including improvements in detector technologies, better dose management, and the development of scale-able systems for routine use.

- **Filtering Techniques:** As the proton energy increases, scattering and angular deviations become more significant. Our findings emphasize that improved filtration methods are essential for maintaining image quality, particularly at higher energies where rejection rates are the highest. Future research should focus on developing more sophisticated energy and angular filtering techniques to minimize data loss while preserving the image clarity.

- **Energy Resolution Trade-offs:** : Improvements in spatial resolution at higher energies come at the cost of WEPL accuracy, especially with current detector limitations. Future studies should focus on enhancing the detector technologies to achieve the required energy resolution for reliable WEPL measurements without compromising the spatial resolution.

- **Cost and Scalability:** The integration of PR systems into clinical workflows faces cost and scalability challenges. While high-energy synchrotrons, such as the helium synchrotron, show potential for delivering the required energies, further research is needed to reduce costs and improve scalability, making PR systems viable for routine clinical practice.

- **Balancing Dose and Image Quality:** As shown in our dose-CNR analysis, balancing the radiation dose with high image quality remains a challenge. Future efforts should concentrate on refining the dose management strategies to achieve optimal image quality while minimizing patient exposure.

LITERATURE REFERENCES

[1] A. A. Pryanichnikov, V. V. Sokunov, and A. E. Shemyakov, in *12th International Scientific Workshop in Memory of Professor V.P. Sarantsev "Problems of Colliders and Charged Particle Accelerators"* (2017).

[2] H. Paganetti, Physics in Medicine & Biology **57**, R99 (2012).

[3] A. C. Knopf and A. Lomax, Physics in Medicine & Biology **58**, R131 (2013).

[4] H.-J. Ziock, K. J. Adams, K. R. Alrick, J. F. Amann, J. G. Boissevain, M. L. Crow, S. B. Cushing, J. C. Eddleman, C. J. Espinoza, T. T. Fife, R. A. Gallegos, J. Gomez, T. J. Gorman, N. T. Gray, G. E. Hogan, V. H. Holmes, S. A. Jaramillo, N. S. P. King, J. N. Knudson, R. K. London, R. P. Lopez, J. B. McClelland, F. E. Merrill, K. B. Morley, C. L. Morris, C. T. Mottershead, K. L. M. Jr., F. A. Neri, D. M. Numkena, P. D. Pazuchanics, C. Pillai, R. E. Prael, C. M. Riedel, J. S. Sarracino, H. L. Stacy, B. E. Takala, H. A. Thiessen, H. E. Tucker, P. L. Walstrom, G. J. Yates, J. D. Zumbro, E. Ables, M. B. Aufderheide, P. D. B. Jr., R. M. Bionta, D. H. Fujino, E. P. Hartouni, H.-S. Park, R. Soltz, D. M. Wright, S. Balzer, P. A. Flores, R. T. Thompson, R. Prigl, J. Scaduto, E. T. Schwaner, A. Saunders, and J. M. O'Donnell, *THE PROTON RADIOGRAPHY CONCEPT*, Tech. Rep. (Los Alamos National Laboratory, Los Alamos, NM 87545, 2010) lawrence Livermore National Laboratory, Livermore, CA 94550; Bechtel, Nevada, Los Alamos Operations, Los Alamos, NM 87545; Brookhaven National Laboratory, Upton, NY 11973; University of Colorado, Boulder, CO 80309; University of Minnesota, Minneapolis, MN 55455; current address: Los Alamos National Lab.

[5] G. Poludniowski, N. M. Allinson, and P. M. Evans, British Journal of Radiology **88**, 20150134 (2015).

[6] M. Petterson, N. Blumenkrantz, J. Feldt, J. Heimann, D. Lucia, A. Seiden, D. C. Williams, H. F.-W. Sadrozinski, V. Bashkirov, R. Schulte, M. Bruzzi, D. Menichelli, M. Scaringella, C. Talamonti, G. A. P. Cirrone, G. Cuttone, D. Lo Presti, N. Randazzo, and V. Sipala, in *IEEE Conference Proceedings* (IEEE).

[7] M. Vretenar, M. E. Angoletta, G. Bisoffi, J. Borburgh, L. Bottura, K. Paļskis, R. Taylor,

G. Tranquille, E. Benedetto, and M. Sapinski, in *13th International Particle Accelerator Conference (IPAC 2022)* (JACoW Publishing, Bangkok, Thailand, 2022).

[8] U. Schneider and E. Pedroni, Radiotherapy and Oncology **110**, 137 (2014).

[9] S. Agostinelli *et al.*, Nuclear Instruments and Methods in Physics Research Section A: Accelerators, Spectrometers, Detectors and Associated Equipment **506**, 250 (2003).

[10] L. Volz, *Proton Radiography and its Applications: Particle imaging for daily in-room image guidance in particle therapy*, Ph.D. thesis, University of Heidelberg (2020), accessed locally.

[11] Geant4 Collaboration, *Geant4 NIST Compounds and Materials* (2024), accessed: 2024-09-10.

[12] C. Johnson, *Treatment Calculations* (Accessed 2024), available at: `https://jeffline.jefferson.edu/Education/programs/radiation_therapy/pdfs/Treatment_Calculations_Johnson.pdf`.

[13] M. G. Herman, J. J. Kruse, and C. R. Hagness, Journal of Applied Clinical Medical Physics **1**, 38 (2000), accessed: 2024-09-10.

[14] Riga Technical University, *Riga Technical University High Performance Computing Cluster (RTU HPC)* (2023), accessed: 2023-09-11.

[15] GEANT4 Collaboration, *Hadronic Physics Lists* (Accessed 2024), chapter 6.5: Physics Lists, GEANT4 Physics Reference Manual.

[16] J. Apostolakis *et al.*, IEEE Transactions on Nuclear Science **53**, 3469 (2006).

[17] GEANT4 Collaboration, *G4EmStandardPhysics_option4* (Accessed 2024).

[18] GEANT4 Collaboration, *G4DecayPhysics* (Accessed 2024).

[19] GEANT4 Collaboration, *G4HadronElasticPhysicsHP* (Accessed 2024).

[20] GEANT4 Collaboration, *G4IonPhysics* (Accessed 2024).

[21] GEANT4 Collaboration, *G4EmExtraPhysics* (Accessed 2024).

[22] C.-A. Collins-Fekete, N. Dikaios, G. Royle, and P. M. Evans, Physics in Medicine & Biology **65**, 085001 (2020).

[23] T. Schneider, L. D. Marzi, A. Patriarca, and Y. Prezado, Frontiers in Physics **9**, 10.3389/fphy.2021.595721 (2021).

[24] C. S. Oria, J. Free, G. G. Marmitt, B. Knäusl, S. Brandenburg, A. C. Knopf, A. Meijers, J. A. Langendijk, and S. Both, Medical Physics **49**, 16208 (2022).

[25] J. K. van Abbema, M.-J. van Goethem, J. Mulder, A. K. Biegun, M. J. W. Greuter, A. van der Schaaf, S. Brandenburg, and E. R. van der Graaf, Nuclear Instruments and Methods in Physics

Research Section B: Beam Interactions with Materials and Atoms **436**, 58 (2018).

[26] C. Sarosiek, E. A. DeJongh, G. Coutrakon, D. F. DeJongh, K. L. Duffin, N. T. Karonis, C. E. Ordoñez, M. Pankuch, V. Rykalin, J. R. Winans, and J. S. Welsh, Journal of Medical Physics **46**, 234 (2021).

[27] W. D. Newhauser and R. Zhang, Medical Physics **42**, 713 (2015).

[28] R. W. Schulte, S. N. Penfold, J. T. Tafas, and K. E. Schubert, Medical Physics **35**, 4849 (2008), first published: 13 October 2008.

[29] L. Eyges, Physical Review **74**, 1534 (1948).

[30] V. L. Highland, Nuclear Instruments and Methods **129**, 497 (1975).

[31] Python Software Foundation, *Python Language Reference, version 3.x* (2023), accessed: 2023-09-11.

[32] T. Plautz, V. Bashkirov, V. Feng, F. Hurley, R. P. Johnson, C. Leary, S. Macafee, A. Plumb, V. Rykalin, H. F.-W. Sadrozinski, K. Schubert, R. Schulte, B. Schultze, D. Steinberg, M. Witt, and A. Zatserklyaniy, Journal of Medical Physics (2014).

[33] R. Fullarton, L. Volz, N. Dikaios, R. Schulte, G. Royle, P. M. Evans, J. Seco, and C.-A. Collins-Fekete, Medical Physics **50**, 2336 (2023), published online 2023 Feb 18.

[34] M. Simard, D. G. Robertson, R. Fullarton, G. Royle, S. Beddar, and C.-A. Collins-Fekete, Physics in Medicine & Biology **69**, 054001 (2024), published on behalf of Institute of Physics and Engineering in Medicine.

[35] M. Prall, M. Durante, T. Berger, B. Przybyla, C. Graeff, P. M. Lang, C. LaTessa, L. Shestov, P. Simoniello, C. Danly, F. Mariam, F. Merrill, P. Nedrow, C. Wilde, and D. Varentsov, Scientific Reports **6**, 27651 (2016), published 10 June 2016.

[36] L. Volz, C.-A. Collins-Fekete, J. R. Sølie, and J. Seco, Biomedical Physics & Engineering Express **6**, 10.1088/2057-1976/ab9c3f (2020).

[37] J. Seco, M. Oumano, N. Depauw, M. Dias, and R. Teixeira, Medical Physics **39**, 3647 (2012), sU-E-I-97: Characterizing the MTF of Proton Radiography.

[38] N. Azadegan, M. Hassanpour, M. U. Khandaker, M. R. I. Faruque, K. Al-mugren, and D. Bradley, Radiation Physics and Chemistry **183**, 109427 (2021).

[39] R. Kataura, T. Izumikawa, T. Konno, and T. Kawasaki, Nuclear Instruments and Methods in Physics Research Section A: Accelerators, Spectrometers, Detectors and Associated Equipment **1027**, 166316 (2022).

[40] R. P. Johnson, Reports on Progress in Physics **81**, 016701 (2018).

[41] R. P. Johnson, Physics in Medicine & Biology **69**, 11TR02 (2024), published on behalf of Institute of Physics and Engineering in Medicine.

[42] F. Longhitano, D. L. Presti, D. L. Bonanno, D. G. Bongiovanni, E. Leonora, N. Randazzo, S. Reito, V. Sipala, and G. Gallo, Nuclear Instruments and Methods in Physics Research Section A **845**, 486 (2017).

[43] J. Takatsu, E. R. van der Graaf, M.-J. van Goethem, M. van Beuzekom, T. Klaver, J. Visser, S. Brandenburg, and A. K. Biegun, Journal of Instrumentation **11**, C01004, published in Journal of Instrumentation, Volume 11, Article 01004.

[44] D. L. Presti, S. Aiello, D. L. Bonanno, G. A. P. Cirrone, E. Leonora, F. Longhitano, C. Pugliatti, N. Randazzo, F. Romano, G. V. Russo, M. Russo, C. Stancampiano, V. Sipala, and T. O. Collaboration, Nuclear Instruments and Methods in Physics Research Section A: Accelerators, Spectrometers, Detectors and Associated Equipment **737**, 195 (2014).

[45] G. Tambave, J. Alme, G. G. Barnaföldi, R. Barthel, A. van den Brink, S. Brons, M. Chaar, V. Eikeland, G. Genov, O. Grøttvik, H. E. S. Pettersen, Z. Pastuovic, S. Huiberts, H. Helstrup, K. F. Hetland, S. Mehendale, I. Meric, Q. W. Malik, O. H. Odland, G. Papp, and S. Yang, Nuclear Instruments and Methods in Physics Research Section A **958**, 162626 (2019).

[46] R. P. Johnson *et al.*, in *IEEE Conference Proceedings* (2015) presented at IEEE Nuclear Science Symposium and Medical Imaging Conference (NSS/MIC), 2015.

[47] I. Tendler, D. Robertson, C. Darne, R. Panthi, F. Alsanea, C.-A. Collins-Fekete, and S. Beddar, Physics in Medicine & Biology **66**, 144001 (2021), focus on Early Career Researchers in Physics in Medicine and Biology.

[48] H. Liu and J. Y. Chang, Radiotherapy and Oncology 10.5732/cjc.010.10529 (2014).